UNIVERSITÀ DEGLI STUDI DI PARMA

DIPARTIMENTO DI FISICA

Numerical Study of Dynamical Instability of Isolated Objects in General Relativity

Giovanni Corvino

Thesis submitted for the award of the degree of Ph.D. in Physics

Dottorato di Ricerca in Fisica

Supervisor: Dott. Roberto De Pietri

XX Ciclo - Gennaio 2009

to the child
who believed
in his dreams

Contents

ACKNOWLEDGEMENTS

I really thank all of those that helped me in the work for this thesis. Thus I say thank you first of all to my supervisor Roberto de Pietri, then I have to thank also Alessandro Nagar, that helped a lot, and in many respects. A big thank you goes to Luciano Rezzolla and all the Albert Einstein Institute numerical relativity group and staff which supported me in the last year of work and gave an important boost to my research. A particular thanks to all the Cactus and Whisky developers team and to the members of the IT department here at the AEI. Finally I thank also INFN and the Department of Physics of the University of Parma for support.

Abstract

This thesis is about instabilities of isolated astrophysical compact objects. The purpose is to study those instabilities through 3D numerical simulations. The first system we deal with are differentially rotating neutron stars for which we focus our attention on the so called "bar-mode" instability, the second one are thick accretion discs around neutron star. For this second system we investigate some features of accretion flows on non rotating neutron stars in view of the future study of accretion driven collapse of such objects.

Differentially rotating neutron stars are known to be unstable to the growth of non axysymmetric modes when restricted to incompressible fluids and Newtonian gravity [21]. In recent years this treatment has been improved to include the full Einstein's equations and a polytropic equation of state [14], [48]. The results concerned the value of the instability parameter β (defined as $\beta = T/|W|$ i.e. the ratio between the kinetic and gravitational potential energy) for the bar-mode instability to develop and the influence on this value of various numerical factors and, more important, of the compactness of the star. What we plan to do is to extend these results to include a more realistic treatment of the fluid via the use of a so-called "realistic" equation of state. These equations of state result from nuclear physics calculations and are meant to be a good approximation to matter near to nuclear densities. In particular we focus on the effect of this kind of EOS on the dependence of β on the compactness. We simulated 4 models, chosen in a region which we thought was fit for our purposes and found that the instability develops also for realistic EOS, even if with different features with respect to the polytropic EOS case.

Accretion discs are very common objects in astrophysics. They stand at the basis of many scenarios and models, the most famous of them being the "fireball

shock" model to explain the GRB's. Here we plan to study the accretion driven collapse of a neutron star to a black hole, which, on the contrary of the accretion induced collapse of a white dwarf to a neutron star, is a not so well studied phenomenon. We generate initial data with the code TORERO written by the author to generate thick accretion discs following the well established theory of stationary configurations of such objects [28], [42]. In the evolution the first thing that shows up is the difference between accretion onto a black hole with respect to a neutron star. In our case matter bounces off the star surface leading to an oscillatory behaviour. In simulating the evolution of the system we keep track also of another instability that affects accretion discs: the runaway instability. This instability is related to the structure itself of equilibrium configurations and consists in a sudden collapse of the whole disc on the central object due to the change in the potential which in turn is caused by accretion. This instability has been widely studied over the years and is of interest here because it could change dramatically the evolution of the system. The main aspects that we want to investigate are the effects of the accretion process on the timescales of the collapse and the properties of the eventual remnant.

Chapter 1

Introduction

Numerical relativity is a field of research that has undergone a big boost in the last few years due to the solution of many problems that had affected it and to the availability of new and powerful computational facilities. Starting from being focused on physical systems that were expected to emit big amounts of energy in gravitational radiation it is now coming to more complex problems involving also the interaction of matter and magnetic fields. Numerical relativity, thus, is nowadays more than in the past a peculiar research field in which knowledge is required from different branches of physics such as electromagnetism and microphysics (for example neutrino physics) that become important to run and to understand the results of the simulations and obviously good programming skills.

The search for gravitational waves (GW) is one of the main challenges of modern physics both from the scientific and technological point of view. The main reason for the hardness of this challenge is the extreme weakness of the expected signal. To have some chance to detect a wave it was then necessary to develop a very sophisticated data analysis algorithm in which a key ingredient was an expected waveform to seek inside the output signal of the interferometers. For this reason the search for GW has been the engine behind the bigger part of the research in numerical relativity for these years of growth of the field. The reached design sensitivity and the plans for contemporary scientific runs at the interferometers has pushed the need for waveforms to be injected in the data analysis algorithm so leading to the main breakthroughs in the field.

From the technical point of view the implementation of the so-called HRSC

methods [31] for the matter evolution equation and the development of the BSSN formulation of the Einstein equation [16],[68] lie at the basis of the big boost mentioned before. After these developments it was possible to solve the binary black hole (BBH) problem, simulating the merger of the two black holes for a sufficient number of orbits in a stable manner. The solution of this problem some year ago [61],[20],[15],[25] was a big success of numerical relativity and following from that result, today many groups in the world collaborate to produce the most reliable waveform, with many improvements that have been produced over the year.

Another important system that has been subject to many studies is the neutron star binary (BNS). This system is believed to be the origin of many astrophysical sources of gravitational and electromagnetic signals like for example GRB's. The basics of the merger of these kind of binaries are now quite well established, due to the work of many groups [12], [51], [70] which investigated deeply this system in various respects like the kind of remnant that one can expect (single black hole or neutron star or accretion disc-central object system) depending on the initial status, the associated gravitational emission and the timescales for the various phases of the evolution (inspiralling, merge, meta-stable state, collapse). All this work has produced a very large number of predicted waveforms and at present BBH waveforms are mature to be injected in data analysis algorithms and BNS signals are getting to the point.

From a purely physical and general point of view the gravitational waves are produced by any phenomenon that affects the quadrupole momentum of the system. The typical one is a non-isotropic (for example non-axysymmetric) instability. In this respect all of the astrophysical systems that are thought to develop such an instability can be of interest for this search. As just said many of these are (and have been) subject of study in numerical relativity but also many are there still to be well understood mainly because there are a lot to be studied. In particular there is still poor work on the effect of instabilities on magnetic field due to the very young age of the code that handle them in strong gravitational field regime.

Another aspect that is worth stressing of the interest in the study of generic instabilities of astrophysical objects is that often the deep understanding of these phenomena can shed light on some particular feature of more complex system that

are expected to be strong sources of GW and in which the instability plays a minor role. An example that is considered in this thesis is the "bar-mode" instability, that consists of a non axysymmetric deformation of a differentially rotating neutron star: a star subject to this instability is itself a source of gravitational radiation, thus justifying the interest in this study, but matter configuration analogous to the ones developed by such a star are found in the final phase of a BNS merge just before the formation of a black hole, so adding interest to the deep understanding of this instability.

The codes used to generate waveforms and in general data to be compared with astrophysics are continously updated and upgraded to let the simulations be as realistic as possible. For example in the last few years many efforts have gone in including magnetic fields in the simulations [33],[69],[26] and improve the treatment of the fluid using realistic equations of state (EOS) [17],[34],[71],[58], these two last points being very important expecially for the BNS problem in which magnetic fields are expected to play an important role and a precise modeling of the microphysics of the fluids is necessary.

This thesis is about two different systems: the first one are differentially rotating neutron stars. Concerning this system we study the effect of a better treatment of microphysic of the fluid on the features of the already mentioned "bar-mode" instability. The second system are thick accretion discs around neutron stars. For this system we concentrate on accretion flow on non rotating neutron stars with the plan to use these information in the near future to study the accretion driven collapse of such objects.

Bar-mode instability of differentially rotating neutron star Differentially rotating neutron stars are well-known systems, they have been studied with many different approaches and targets. Equilibrium models have been studied in detail [40],[41],[22],[76] and also works including magnetic field put some light on, in particular on oscillation modes [74],[75]. The instability that is in our interest here is the so called "bar-mode" instability. This instability consists in a deformation of the rotating star that assumes an ellipsoidal shape (i.e. the "bar" shape). It can be explained in terms of linear coupling of non-radial axial modes with an azimuthal dependence $e^{im\phi}$ (with $m = 1, 2, ...$) that leads to an exponential growth of the

$m = 2$ one. This happens when the instability parameter $\beta \equiv T/|W|$ (i.e. the ratio between the kinetic and the gravitational potential energy) reaches a critical value. The only comprehensive and rigorous study of this kind of instability has been done for incompressible self-gravitating fluids in Newtonian gravity [21], [65] but a complete treatment of this instability requires three dimensional simulations in full-gr to understand its behaviour in the non-linear regime and the determination of the threshold.

Despite this requirements only in recent years a wide study of it has been conducted in full-gr with star models computed solving Einstein's equation coupled to matter [14], going beyond all the works done with Newtonian and post-newtonian treatment of gravity. These works, though approximations, gave a good insight in the phenomenon that could not have been reached with a perturbative treatment. In particular the results of these studies showed that the critical value β_c depends weakly on the EOS and that the formation of spiral arms is fondamental in redistributing the angular momentum once the bar has formed [27],[36],[73],[56],[46],[78],[19],[35],[55]. More recently it was also shown that a high degree of differential rotation could lower the value of β_c and a weak dependence on the EOS was confirmed [60],[79],[37],[66],[67]. The cronologically last thing that these Newtonian analysis have shown is that an $m = 1$ mode plays an important role with smaller values of β. These instabilities are called "low-β" instabilities [59], [62] and will not be treated here.

Here we plan to extend results in in [14] and [48] improving the models with respect to the microphysics. In particular we plan to move from the polytropic or ideal gas EOS used there to a realistic EOS so to include some microphysics in the physical setup for the simulations. From the physical point of view we want to address the effect of the EOS on the dependence of β on the compactness. The EOS we plan to use, described in detail in section 3.1, are EOS of the so called "unified" kind, meaning that are built up from other realistic EOS to cover a wide range of densities and be suitable to model nuclear matter.

What we find from our study, first of all, is that also with a realistic EOS the star is deformed and assumes a bar shape. The analogies with the polytropic case more or less stop here since the general beaviour of the star is much different. In our simulations we find an $m = 3$ mode growing after the $m = 2$ one and becoming

the dominant one in contrast with the polytropic case in which the first mode to grow after the bar deformation was the $m = 1$. Another aspect in which the bar-mode instability with realistic EOS differs from polytropic is that the deformation is much smaller and the spiral arms are much thinner. We simulated 4 models of rotating star and found that all of them are unstable with respect to the bar-mode instability thus telling that the critical value for the realistic EOS we used is lower than the one for the polytropic, more precisely it must be less than $\beta_c = 0.241$ which is the lower value we simulated.

Microphysics in numerical relativity The microphysics of the fluid is an aspect of the simulations that has still to be treated with a sufficient accuracy in 3D full-gr numerical calculations. With our numerical method the peculiarities of the fluid are encapsulated in the equation of state that closes the system of equation to be solved by the code. The first approximation used still in a big part of works is the polytropic or the ideal gas equation of state in which, respectively, $p = K\rho^{\Gamma}$ or $p = \rho\epsilon(\Gamma - 1)$, with K and Γ constants and where p, ρ and ϵ are pressure, rest-mass density and internal energy density. These two equations of state, being a first approximation, give just a first look to the real physics of the phenomena but nonetheless proved to be very useful in this task giving thrustful results. A first step towards a satisfactory treatment of the fluid is given by the so called realistic equations of state. These EOS are computed from effective hamiltonians including various quantum effects and offer a very wide range of possibilities to explore for many purposes. For example there is a strong dependence on the EOS used in the mass-radius relation of neutron stars and thus numerical data on emissions from astrophysical sources can be combined with real data to constrain the radial extension of the star from the EOS and vice-versa. Another aspect that has to be stressed to understand why the realistic EOS have been introduced in numerical relativity only in recent years is the computational cost. When the EOS is actually implemented in the code it is made of a number of routines that compute a thermodynamic quantity starting from others. These routines are called many times for each point of the grid and at each time step so if you go from a simple analytic expression like the polytropic EOS that needs only one line of code to something more complicated (even a few lines) the overall computational cost is

dramatically increased and only in recent years clusters powerful enough become available to make such a simulation.

We implemented in the Whisky code routines to compute two different equations of state taken by literature: a barotropic or "cold" one [34] that allows no schock heating, and a non barotropic one [71]. We tested against convergence on a simple spherically simmetric star (TOV) and we found that the EOS described in [34] had to be modified to ensure convergence on the code and thus to use those routines for simulations of the bar-mode instability that is our goal.

Accretion discs around non rotating neutron stars Accretion discs in astrophysics have an important role in models that are at the basis of many scenarios [45], [77], [32]. For example astrophysical sources that imply a collimated jet are based on the presence of a disc that funnels particles and radiation along the rotation axis, another example is the model of the central engine of short GRB that is believed to be made of a BH-disc system. Besides these ones just mentioned models developed to explain millisecond pulsars or LMXB often comprise a disc as a fondamental component. Over the years different models of accretion discs have been developed with many different features for example the Shakura and Sunyaev model [64] that is at the basis of the accretion models from thin discs or thick discs that were studied starting from the 70's [28],[42] or more recently advection dominated accretion flows [53],[54] that were introduced to explain rotation rates of neutron stars.

Our main goal is to study the accretion driven collapse of neutron stars to black holes. This instability has been thoroughly studied in the case of a white dwarf (WD) collapsing to form a neutron star. Some of these studies [43],[44], for example, focused on the explanation of the very short rotation period of millisecond pulsars through accretion on a WD of rotating matter from a disc. Also many models of low mass X-ray binaries (LMXB) imply the presence of a compact star surrounded by an accretion disc that is fuelled by a companion giant star. The case of the collapse of NS to a black hole (BH) is instead much less studied, leaving many aspects still to be understood. Our plan is to study the effect of the accreting matter on the dynamics of the collapse, namely on its timescales and on the possible remnant disc around the BH.

The system we chosed for our simulations is made of a thick disc (torus) around a spherically symmetric star (TOV), we simulated accretion flows with the new code Whisky2D and studied its features. All the informations that we got from our simulations are meant to be used for the future staudy of the actual accretion driven collapse.

Linked to the collapse induced by accretion, another instability of a disc-compact object system has to be considered: the runaway instability. This phenomenon, first studied in the early 80's [6],[80] consists of a sudden collapse of the disc itself on the central object (see section 3.2, in particular 3.2.4) and is a consequence of the nature itself of the equilibrium models of accretion disc. In the study of accretion induced collapse we keep track of the stability of the disc with respect to this particular phenomenon because it could change dramatically the amount of matter that the star can accrete.

The thesis is organized as follows: in chapter 2 we briefly present the systems of equation that we solve to perform the simulations and define the variables we use, in chapter 3 there's the description of the physical systems and of the EOS of our interest. Chapter 4 and 5 are devoted, respectively, to results concerning barmode instability and accretion driven collapse. In chapter 6 we draw the conlusions about our work and depict future efforts to be done.

We use a space-like signature (-,+,+,+), latin indices running from 1 to 3 and greek ones running from 0 to 3. Unless differently stated all the quantities are expressed in geometrical units ($c = G = 1$) with the addictional constraint that the mass of the sun is equal to one.

Chapter 2

Evolution of fields and matter

In this Chapter we briefly review the properties of the codes we used for the evolution to make this thesis more self-consistent. The code we used is the general-relativistic hydrodynamics code Whisky [13] in which the hydrodynamics equations are written as finite differences on a cartesian grid and solved using high-resolution shock-capturing (HRSC) schemes. For the space-time evolution, instead, we use the BSSN formulation of the Einstein equation.

2.1 Evolution of the Einstein equations

The original ADM formulation casts the Einstein equation into a first order (in time) quasi-linear system of equations. The dependent variables are the three metric γ_{ij} and the extrinsic curvature K_{ij}, with first order evolution equations give by

$$\partial_t \gamma_{ij} = -2\alpha K_{ij} + \nabla_i \beta_j + \nabla_j \beta_i, \tag{2.1}$$

$$\partial_t K_{ij} = -\nabla_i \nabla_j \alpha + [R_{ij} + K K_{ij} - 2K_{im} K^m_j \tag{2.2}$$

$$- 8\pi (S_{ij} - \frac{1}{2}\gamma_{ij} S) - 4\pi \rho_{ADM} \gamma_{ij}] \tag{2.3}$$

$$+ \beta^m \nabla_m K_{ij} + K_{im} \nabla_j \beta^m + K_{mj} \nabla_i \beta^m. \tag{2.4}$$

Here α is the lapse function, β_i is the shift vector, ∇_i denotes the covariant derivative with respect to the three metric, $K \equiv \gamma^{ij} K_{ij}$ is the trace of the extrinsic curvature, S_{ij} is the projection of the stress-energy tensor onto the space-like hy-

persurfaces and $S \equiv \gamma^{ij} S_{ij}$. In addition to the evolution equations, the Einstein equations also provide four constraint equations to be satisfied on each space-like hypersurface. These are the Hamiltonian constraint equation

$$^{(3)}R + K^2 - K_{ij}K^{ij} - 16\pi\rho_{ADM} = 0, \tag{2.5}$$

and the momentum constraint equations

$$\nabla_j K^{ij} - \gamma^{ij}\nabla_j K - 8\pi j^i. \tag{2.6}$$

In equations (2.2)-(2.6), ρ_{ADM} and j^i are the total energy density and the momentum density as measured by an observer moving orthogonally to the space-like hypersurfaces.

In particular, we use a conformal traceless reformulation of the above system od evolution equations, as first suggested by Nakamura, Oohara and Kojima [52] (NOK formulation), in which the evolved variables are the conformal factor (ϕ), the trace of the extrinsic curvature (K), the conformal 3-metric ($\tilde{\gamma}_{ij}$), the conformal traceless extrinsic curvature ($\tilde{A}_{ij}$) and the *conformal connection functions* ($\tilde{\Gamma}^i$), defined as

$$\phi = \frac{1}{4} log(\sqrt[3]{\gamma}), \tag{2.7}$$

$$K = \gamma^{ij} K_{ij}, \tag{2.8}$$

$$\tilde{\gamma}_{ij} = e^{-4\phi}\gamma_{ij}, \tag{2.9}$$

$$\tilde{A}_{ij} = e^{-4\phi}(K_{ij} - \gamma_{ij}K), \tag{2.10}$$

$$\tilde{\Gamma}^i = \tilde{\gamma}^{ij}_{,j}. \tag{2.11}$$

The code used to evolve these quantities is the one developed within the Cactus computational toolkit [1] and is designed to handle arbitrary shift and lapse conditions. In particular, we have used hyperbolic K-driver slicings conditions of the form

$$\partial_t \alpha = -f(\alpha)\alpha^2(K - K_0), \tag{2.12}$$

with $f(\alpha) > 0$ and $K_0 \equiv K(t = 0)$. This is a generalization of many well known slicing conditions. For example setting $f = 1$ we recover the "harmonic" slicing condition, while setting $f = q/\alpha$, with q integer, we find the generalized "1+log"

slicing condition [18]. In particular, all the simulations discussed in this thesis are done using condition (2.12) with $f = 2/\alpha$. This choice has been made mostly because of its computational efficiency, but be aware that "gauge pathologies" could develop with the "1+log" slicings [8][10].

As for the spatial gauge, we use one of the "Gamma-driver" shift conditions proposed in [9], that essentially act driving the $\tilde{\Gamma}^i$ to be constant. In this respect, the "Gamma-driver" shift conditions are similar to the "Gamma-freezing" condition $\partial_t \tilde{\Gamma}^k = 0$, which, in turn, is closely related to the well-known minimal distortion shift condition [72].

In particular, all the results reported here have been obtained using the hyperbolic Gamma-driver condition,

$$\partial_t^2 \beta^i = F \partial_t \tilde{\Gamma}^i - \eta \partial_t \beta^i, \tag{2.13}$$

where F and η are, in general, positive functions of space and time. For the hyperbolic Gamma-driver conditions it is crucial to add a dissipation term with coefficient η to avoid strong oscillations in the shift. Experience has shown that by tuning the value of this dissipation coefficient it is possible to almost freeze the evolution of the system at late times. We typically choose $F = \frac{3}{4}\alpha$ and $\eta = 2$ and do not vary them in time.

2.2 Evolution of the hydrodynamics equations

The stellar models are here treated in terms of a perfect fluid with stress-energy tensor

$$T^{\mu\nu} = \rho h u^\mu u^\nu + p g^{\mu\nu} \tag{2.14}$$

where

$$h = 1 + \epsilon + \frac{p}{\rho} \tag{2.15}$$

is the specific enthalpy, ϵ is the specific internal energy and ρ the rest-mass density, so that $e = \rho(1+\epsilon)$ is the total energy density in the rest frame of the fluid. The equations of relativistc hydrodynamics are then given by the conservation laws for

the energy, momentum and baryon number:

$$\nabla_\mu T^{\mu\nu} = 0, \tag{2.16}$$

$$\nabla_\mu (\rho u^\mu) = 0 \tag{2.17}$$

once supplemented with an EOS of the kind $p = p(\rho, \epsilon)$. The hydrodynamic code has been written to use any EOS but here we will use only a polytropic EOS

$$p = K\rho^\Gamma \tag{2.18}$$

or a "realistic" EOS. This kind of EOS will be discussed in detail in chapter 3. For this latter kind of EOS the entropy is not constant and thus the evolution equation for ϵ (that for the polytropic EOS is analytically computed) needs to be solved.

An important feature of the Whisky code is the implementation of a *conservative formulation* of the hydrodynamics equation in which the set of equations (2.16) and (2.17) is writte in a hyperbolic, first-order and flux conservative form of the type

$$\partial_t \mathbf{q} = \partial_i \mathbf{f}^{(i)}(\mathbf{q}) = \mathbf{s}(\mathbf{q}), \tag{2.19}$$

where $\mathbf{f}^{(i)}(\mathbf{q})$ and $\mathbf{s}(\mathbf{q})$ are the flux-vectors and source terms, respectively (see [30] for an explicit form of the equations). Note that the right hand side (the source term) depends only on the metric and it's first derivatives and on the stress-energy tensor. In order to write system(2.16-2.17) in the form of system (2.19), the *primitive* hydrodynamical variables (i.e. the rest-mass density ρ, the internal energy density ϵ and the fluid three-velocity v^i (measured by a local zero-angular momentum observer), the pressure p (measured in the rest frame of the fluid) and the lorentz factor $W = \alpha u^0$ are mapped to the so called *conserved* variables $\mathbf{q} \equiv (D, S^i, \tau)$ via the relations

$$D \equiv \sqrt{\gamma} W \rho, \tag{2.20}$$

$$S^i \equiv \sqrt{\gamma} \rho h W^2 v^i, \tag{2.21}$$

$$\tau \equiv \sqrt{\gamma}(\rho h W^2 - p) - D \tag{2.22}$$

As previously stressed, in the case of polytropic EOS (2.18), one of the evolution equations (the one for τ in our case) doesn't need to be solved as the internal energy density can be readily computed analytically as

$$\epsilon = \frac{p}{\rho(\Gamma - 1)} \tag{2.23}$$

Additional details of the formulation we use for the hydrodynamics equations can be found in [30].

Chapter 3

Physical systems under investigation

In this chapter we explain the detailed features of the systems we are studying, their stability properties and the instabilities they are supposed to develop. we will describe also the equations of state that we want to use and the effect we expect them to have in the systems of interest. In section 3.1 there is an outlook on the present status of the knowledge on bar-mode instability and detail about the EOS we plan to use in our study while section 3.2 deals with equilibrium models of accretion discs and runaway instability

3.1 Barmode instability of rotating neutron stars with realistic equation of state

The last two works on bar-mode instability [48],[14] were addressing the issue on a more general and accurate basis than the ones cited in the introduction that used Newtonian or post-Newtonian approximations to gravity. The code they used, which is the same we are going to use for our study, the Whisky code, is a general relativistic hydrodynamic code, which is coupled to an evolution of space-time that uses the BSSN formulation of the Einstein equation. This setup is the more general possible on the gravitational side and thus the results of the study were very accurate. Going into details there were a number of question that the authors addressed and to which they gave an answer. The main results were the computation of the threshold value $\beta_c = 0.255$ and the study of the dependence

of this value on the compactness of the star that had been predicted from post-Newtonian studies [63]. Other outcomes were about the effect of symmetries, resolution, initial perturbations and EOS were considered with results that can be summarized as:

- an initial perturbation introduced ad hoc in the initial data influences the duration of the bar-mode deformation but not its growth time.
- symmetries other than reflection on the x-y plane can influence the dynamics dramatically, expecially near the threshold.
- the persistence of the bar depends strongly on the degree of overcriticality
- non linear mode coupling is the main cause of bar suppression
- the bar-mode deformation for largely overcritical models is mainly suppressed through the conversion of kinetic energy into internal one.
- the presence of shocks (allowed with a non-isentropic EOS) does not affect the dynamics considerably.
- the compactness of the star changes the threshold value for bar-mode instability growth.

As said in the introduction our main interest is the study of the influence of the EOS on the dependence of the β parameter on the compactness that has been studied in [63],[48]. Equilibrium models of rotating star generated with realistic EOS are much more compact than the ones generated with the polytropic one and thus we expect an effect of the EOS on this dependence. This aspect of the realistic stars will be discussed in section 4.1 when dealing with the choice of interesting initial models for bar-mode instability simulations. We concentrate here on the features of the EOS we use.

The realistic equations of state are the result of nuclear physics calculations. In these calculations different effects are accounted for and the final outcome is a table of values of thermodynamic variables. The main problem in handling these tables is the interpolation between points that can introduce additional errors to the ones originally contained in the model that is at the basis of the table computation.

Many different interpolation techniques exist but there's also another way of facing this issue: different authors developed analytic fits to tables to overcome the choice of the best interpolation technique. We implemented the analytic fits described in [34] (HP fit) and [71] (Shibata fit). These two fits, besides being two of the few existing that cover a sufficient range of densities, have been already used in numerical computations and thus we choosed this mainly to let our results be comparable with the literature.

3.1.1 The HP fit

This fit is made on two different equations of state, of the "unified" kind. They are both zero temperature (cold) equations of state and thus they don't admit shock heating, or, stated differently, p is a function of only ρ or ϵ. For this reason we will refer to this fit as to a "cold" fit. These EOS are called "unified" because the different ranges in the table are handled with different equations of state, each one of them being the best approximation in that range. In this case the different equations of state used are:

- BPS (Baym et al. 1971) for densities $e \leqslant 10^8 g/cm^3$
- HP94 (Haensel & Pichon 1994) in the range $10^8 \leqslant e \leqslant 5 \times 10^{10} g/cm^3$
- FPS or SLy for $e \geqslant 10^{10} g/cm^3$, this part differentiates the two "unified" EOS fitted so we will refer to as FPS or SLy fit accordingly

and the fit is made by means of an exponential function, namely:

$$f_0(x) = \frac{1}{e^x + 1} \tag{3.1}$$

This function is used to fit the pressure p as a function of total energy density e in the following way (the a's are the fit's coefficients):

$$\begin{aligned} \zeta = & \frac{a_1 + a_2\xi + a_3\xi^3}{1 + a_4\xi} f_0(a_5(\xi - a_6)) + \\ & + (a_7 + a_8\xi) f_0(a_9(a_{10} - \xi)) + \\ & + (a_{11} + a_{12}\xi) f_0(a_{13}(a_{14} - \xi)) + \\ & + (a_{15} + a_{16}\xi) f_0(a_{17}(a_{18} - \xi)) \end{aligned} \tag{3.2}$$

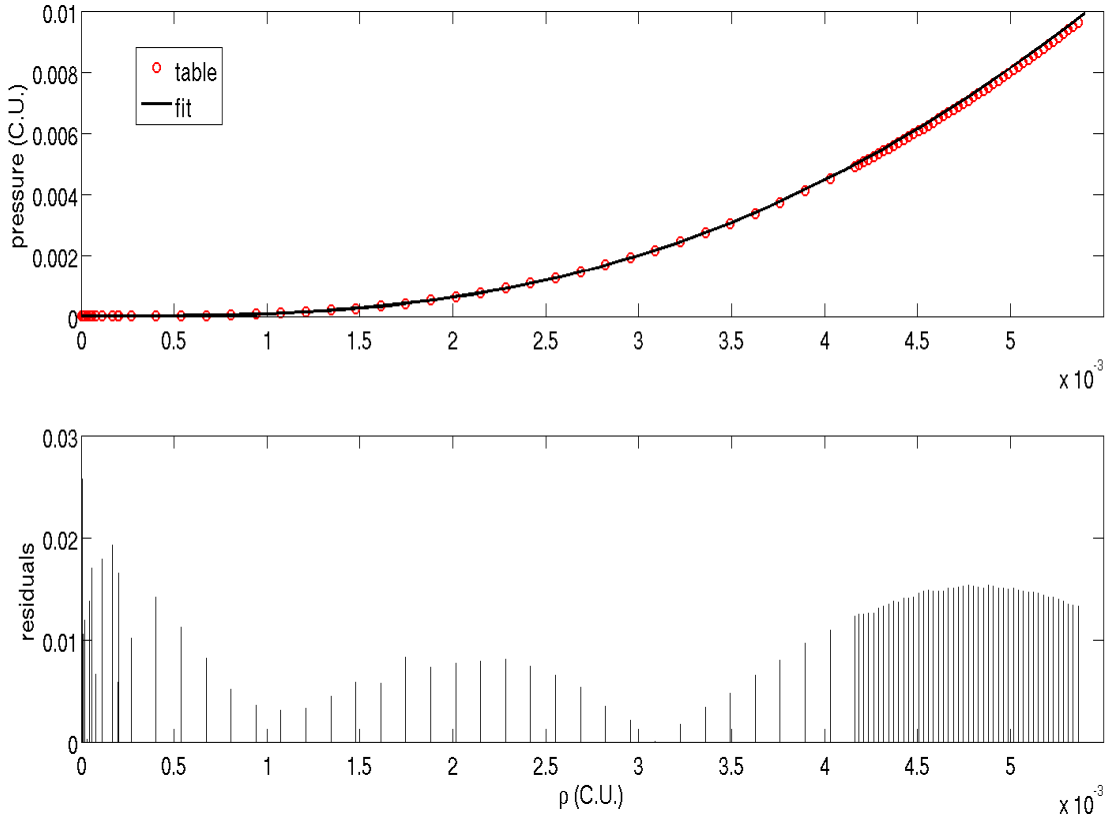

Figure 3.1: **Upper panel**: pressure as a function of rest-mass density for fit 3.2 (solid line) and for the EOS table (circles). **Lower panel**:residuals

where $\xi = log(e)$, $\zeta = log(p)$ and e and p are in cgs units. The two sets of coefficients for the FPS and SLy fit that we're describing are given in [34] and we did not touch them at all, so the interested reader can easiliy find them there. Once the pressure is computed in our runs, we need the internal energy density ϵ. Again we have a fit of the same kind:

$$\epsilon = \frac{p_1\rho^{p_2} + p_3\rho^{p_4}}{(1+p_5\rho)^2} f_0(-p_6(log(\rho)+p_7)) + \\ + \frac{\rho}{8\times 10^{-6} + 2.1\rho^{0.585}} f_0(p_6(log(\rho)+p_7)) \tag{3.3}$$

The maximum error that these fits give with respect to the tables is of about 3% as shown in figure 3.1 for fit 3.2 on SLy table.

3.1.2 The Shibata fit

Also in this case we have two different fits, made on the same "unified" equations of state of the HP fit. The main difference is that in this case pressure and internal energy are handled so to admit also a thermal component, i.e. pressure and thermal energy are written in the form:

$$p = p_{cold} + p_{th} \tag{3.4}$$

$$\epsilon = \epsilon_{cold} + \epsilon_{th} \tag{3.5}$$

The fitted quantity is only the cold part of the internal energy density ϵ_{cold} as a function of the rest mass density ρ:

$$\begin{aligned}\epsilon_{cold}(\rho) = &[(1 + p_1\rho^{p_2} + p_3\rho^{p_4})(1 + p_5\rho^{p_6}) - 1]f_0(-p_8\rho + p_{10}) + \\ &+ p_{12}\rho^{p_{13}} f_0(p_8\rho - p_{10})f_0(-p_9\rho + p_{11}) + \\ &+ p_{14}\rho^{p_{15}} f_0(p_9\rho - p_{11})\end{aligned} \tag{3.6}$$

where the p_i are the coefficients of the fit (also here two sets of coefficients). The cold part of the pressure p_{cold} is the computed by means of:

$$p_{cold} = \rho^2 \frac{d\epsilon_{cold}}{d\rho} \tag{3.7}$$

This is another difference worth stressing between the HP and the Shibata fit: this last relation comes from the first principle of thermodynamics while in the HP case both p and ϵ were fitted. The actual difference in the values of p between the two fits is less than one percent but while this one strictly fullfills the first principle of thermodynamics (although on fitted values) the HP one is more accurate on the table and thus both have advantages and disadavantages. An interesting consequence of the unconsistency of the HP fit is discussed in section 4.2.

The thermal part of the fluid is treated with an ideal-gas equation of state:

$$p_{th} = (\Gamma_{th} - 1)\rho\epsilon_{th} \tag{3.8}$$

where $\epsilon_{th} = \epsilon - \epsilon_{cold}$. The reason why this kind of hybrid equation of state is of some interest is that while a single neutron star can be well modeled by a cold eos, in a merger, or in a highly dynamical situation, shocks can form and thus is preferrable to have a way to heat up the fluid because of these shocks. Nevertheless the thermal part is expected to be smaller than the cold one [71].

3.2 Accretion discs around compact objects

The kind of disc that we describe here is the so called neutron torus or thick disc. This naming is in contrast with the thin disc models for which there's no pressure and the dynamic of the system is keplerian. Here, instead we have the disc that extends also out of the equatorial plane leading to a matter configuration in which pressure gradients play an important role.

An accretion disc is made by matter orbiting around a compact central object (BH or NS) in an axysymmetric configuration, the equilibrium is given by the balance between centrifugal and gravitational forces and this balance results in an effective potential. The detailed features of this potential depend obviously on the physical parameters of the system but there are some qualitative features that are interesting for our purposes and need to be stressed, namely the presence of a well in which the matter is in stable equilibrium and of a cusp, that marks the division between open and closed equipotential surfaces in the plane that comprises the rotation axis.

Depending on the absolute value of the potential at the inner edge, a disc is said to be stable if the value is less than the value at the maximum (cusp), marginally stable if it is equal to that value and unstable if it is bigger. The presence of the well is thus crucial for the existence of stable discs.

The cusp has its importance when dealing with the evolution of a disc of the unstable or marginally stable type. Being the result of balance between gravitational and centrifugal forces, the position of this point in the equatorial plane is influenced by any change in the distribution of matter. An accretion process is the tipical one to make such a job. The question whether the cusp moves inward or outwards during the accretion is a fondamental one, because upon it also depends the stability of the torus: suppose that the initial configuration consists of an unstable torus, this torus will clearly accrete matter on the central object, if the cusp will move towards it the net effect of this motion will be to decrease the rate of accretion and eventually stop it, leading to a stable configuration. On the other side a motion of the cusp outwards will speed up the process leading to a collapse of the disc. This process is the runaway instability.

The presence of the cusp and of the well depends on the value and the distri-

bution of angular momentum of the matter.

Before describing the instability and its features through a review of the main works done in the past on it, I will describe the theory of equilibrium configuration of the accretion discs under consideration. The theory of equilibrium configurations of these objects has been developed starting from the second half of the 70's [28, 42, 5], and is based on a black hole as central object. Though the applications of this models and the results that will be discussed in chapter 5 refer to a spherically symmetric star, we expose the theory as it was originally formulated, reminding that as far as one is restricted to spherical symmetry the theory is the same.

In what follows we assume geometrical units ($c = G = 1$) and a space-time signature $-+++$. The thermodinamical quantities are: p for the pressure, ρ the rest mass density, ϵ the specific internal energy, $e = \rho + \epsilon$ is the total energy, $h = (e+p)/\rho$ the specific enthalpy. We use greek indices spanning from 0 to 3 and latin ones from 1 to 3.

The theory of stable configurations is based on some physical assumptions, namely:

- the space-time is stationary and axysymmetric (i.e. the metric does not depend on t and ϕ). We adopt coordinates (t, r, θ, ϕ) in which the metric has the form:

$$ds^2 = g_{tt}dt^2 + 2g_{t\phi}dtd\phi + g_{\phi\phi}d\phi^2 + g_{rr}dr^2 + g_{\theta\theta}d\theta^2 \tag{3.9}$$

- the fluid is isentropic ($p = p(\rho)$), here we will use a polytropic EOS, i.e. $p = \kappa\rho^\Gamma$ where κ and Γ are the polytropic constant and the polytropic exponent.

- the flow of the fluid is purely azimuthal so that the 4-velocity can be written as $u^i = \left(u^t, 0, 0, u^\phi\right)$ with the normalization condition:

$$u^2 = u^\mu u_\mu = -1. \tag{3.10}$$

- the self-gravity of the disc is neglected, the space-time is used as a background for the Euler equations.

In constructing equilibrium models under this assumptions only one unknown function remains to be given: the distribution of angular momentum in the equatorial plane $l_{eq} = l_{eq}(r)$ and thus we will focus on this distribution, that determines the shape of the equipotential surfaces, to describe the details of the configurations.

3.2.1 Definitions

- Angular momentum: we define the angular momentum per unit inertial mass as:

$$l = -\frac{u_\phi}{u_t} \tag{3.11}$$

and the corresponding angular velocity as:

$$\Omega = \frac{u^\phi}{u^t} \tag{3.12}$$

From $u_\mu = g_{\mu\nu}u^\nu$ it follows that they are related through:

$$l = -\frac{g_{t\phi} + g_{\phi\phi}\Omega}{g_{tt} + g_{t\phi}\Omega} \ , \ \Omega = -\frac{g_{t\phi} + g_{tt}l}{g_{\phi\phi} + g_{t\phi}l} \tag{3.13}$$

This definition of angular momentum is not unique but is the most reasonable for our purposes; other viable choices are for example $l = -u_\phi$ or $l = -u_\phi u^t$ which have all the same newtonian limit but suffer from other defects as the absence of a clear stability criterion (which in this case is simply $dl/dr > 0$) or the fullfillment of the von Zeipel's theorem [42].

- von Zeipel's cylinders: they are defined as surfaces of constant l and Ω. These two surfaces coincide only in the case of a barotropic equation of state [2, 3, 4]. The equation of the cylinder corresponding to a certain value of l is obtained, if the metric is known, from eqs.(3.13). As an example in figure 3.2 is shown the shape of the von Zeipel's cylinder for a spherically symmetric metric.

- equipotential surfaces: the potential that determines the motion of the fluid is the following:

$$W - W_{in} = -\int_0^p \frac{dp}{h\rho} = ln\left(\frac{h}{h_{in}}\right) \tag{3.14}$$

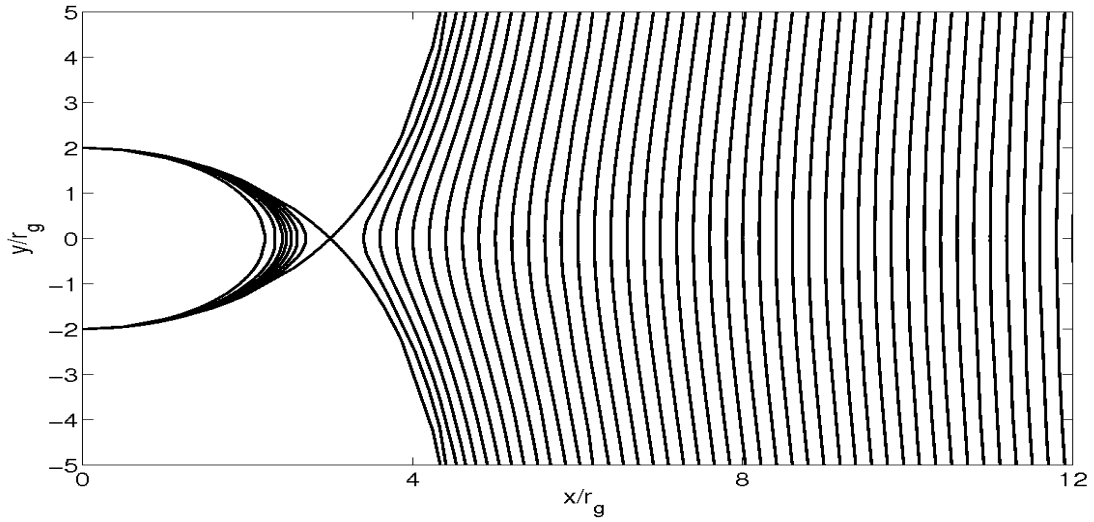

Figure 3.2: von Zeipel cylinders for the Schwarzschild metric, each line refers to a different value of the angular momentum

This potential, from the integral form of the Euler equation can be written:

$$W - W_{in} = ln(-u_t) - ln(-u_{t,in}) - \int_{l_0}^{l} \frac{\Omega dl}{1 - \Omega l} \tag{3.15}$$

where, here and after, the subscripts *in* and *out* refer respectively to the inner and outer edge of the disc. The constant W_{in} can be eliminated imposing that $W(r, \theta) \to 0$ for $r \to +\infty$. An example of equipotential surfaces is in figure 3.3.

- energy per unit inertial mass: from the normalisation condition (3.10) it follows that the energy per unit inertial mass $-u_t$ can be expressed as a function of the angular momentum as

$$-u_t = \sqrt{\frac{\bar{\omega}^2}{g_{tt}l^2 + 2g_{t\phi}l + g_{\phi\phi}}}. \tag{3.16}$$

where $\bar{\omega} = g_{t\phi}^2 - g_{tt}g_{t\phi}$.

3.2.2 Equilibrium configurations with $l = const$

This section is devoted to the simple case in which $l_{eq} = l_0$ with l_0 constant and the space-time is spherically symmetric. The presence of a cusp and of a center in

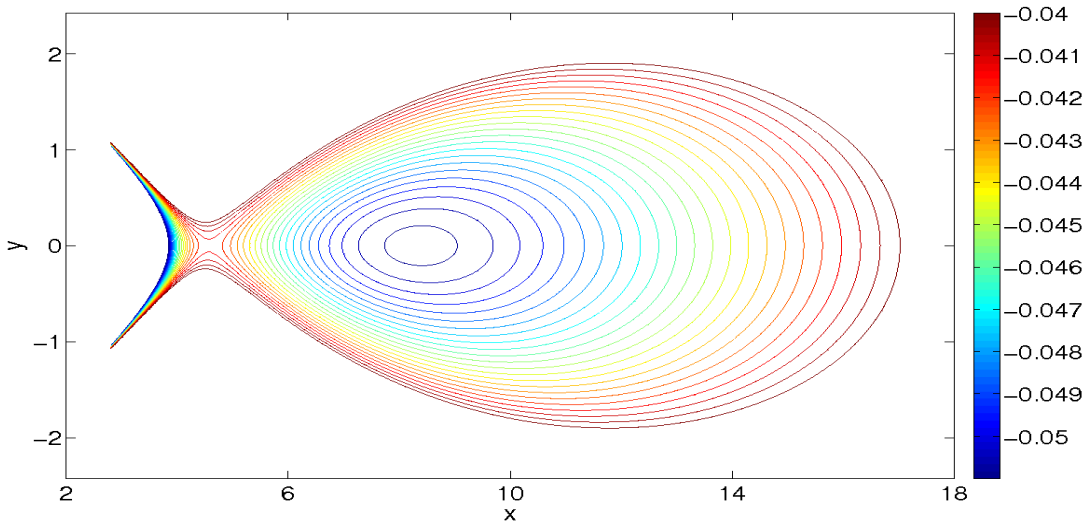

Figure 3.3: Equipotential surfaces for a Schwarzschild metric and $l = 3.8$, computed with expression 3.15

the equatorial plane of the disc depends on the solution of the equation

$$l_{K,eq}(r) = l_{eq} \tag{3.17}$$

This can be proven matematically [23]but has also a simple physical explanation: by definition the angular momentum of an orbit is keplerian if the gravitational and centrifugal forces are exactly balanced. This can happen at a minimum of the potential (where the pressure gradient vanishes) or at a maximum (where there's the edge of the disc or no matter). The maximum and the minimum correspond to the cusp and the center of the disc. In our case the keplerian angular momentum is given by:

$$l_{K,eq} = \frac{r\sqrt{r}}{r-2} \tag{3.18}$$

Corresponding to the minimum of this function (radius of the marginally stable orbit r_{ms}) and to the radius r_{mb} where a fluid element becomes unbound (i.e.$-u_t < 1$), we can compute two values of the angular momentum that determine the range of interest for us. These two values are:

$$l_{ms} = \frac{3\sqrt{6}}{2} \approx 3.67 \ , \ l_{mb} = 4 \tag{3.19}$$

Depending on the values of l the equipotential surfaces will have different geometry and the configuration will have or not a cusp and a centre. It is clear from the

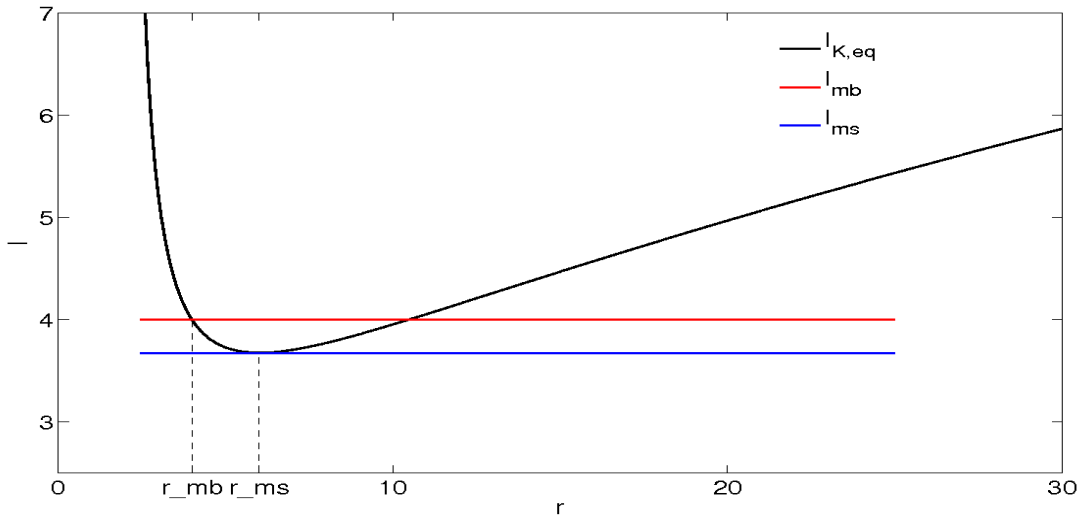

Figure 3.4: Keplerian angular momentum values in the equatorial plane, marginally stable value (blue) and marginally bound value (red)

pictures below (figs [3.5]-[3.9]) that the case of interest is the one with $l_{ms} < l_0 < l_{mb}$ because we have distinct cusp and center and the equipotential at the cusp is closed at a finite radius.

From the equation of state that we use and from the expression (3.14) for the potential we can compute the thermodynamic quantities that we need:

$$p = \kappa \left(\frac{\Gamma - 1}{\Gamma} \frac{e^{W_{in} - W} - 1}{\kappa} \right)^{\frac{\Gamma}{\Gamma - 1}} \quad , \quad \rho = \left(\frac{\Gamma - 1}{\Gamma} \frac{e^{W_{in} - W} - 1}{\kappa} \right)^{\frac{1}{\Gamma - 1}} \tag{3.20}$$

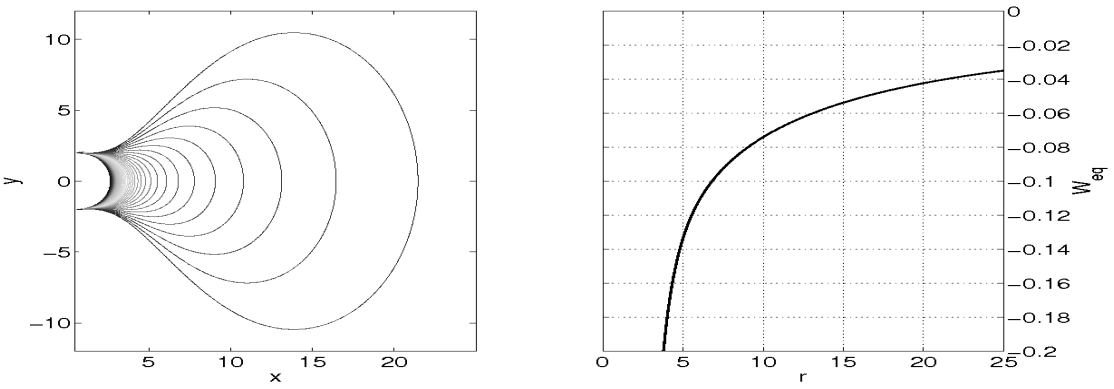

Figure 3.5: Equipotential surfaces and potential in the equatorial plane for $l = 3$

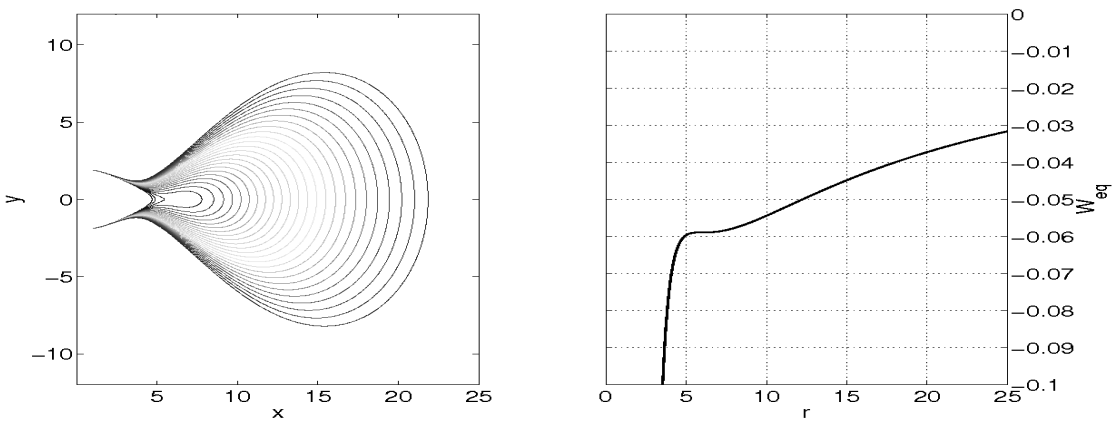

Figure 3.6: Equipotential surfaces and potential in the equatorial plane for $l = l_{ms}$

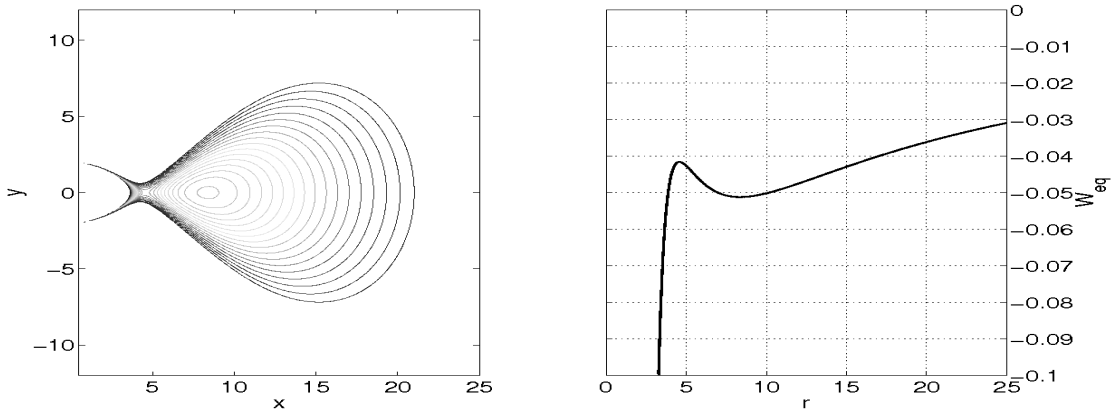

Figure 3.7: Equipotential surfaces and potential in the equatorial plane for $l = 3.8$

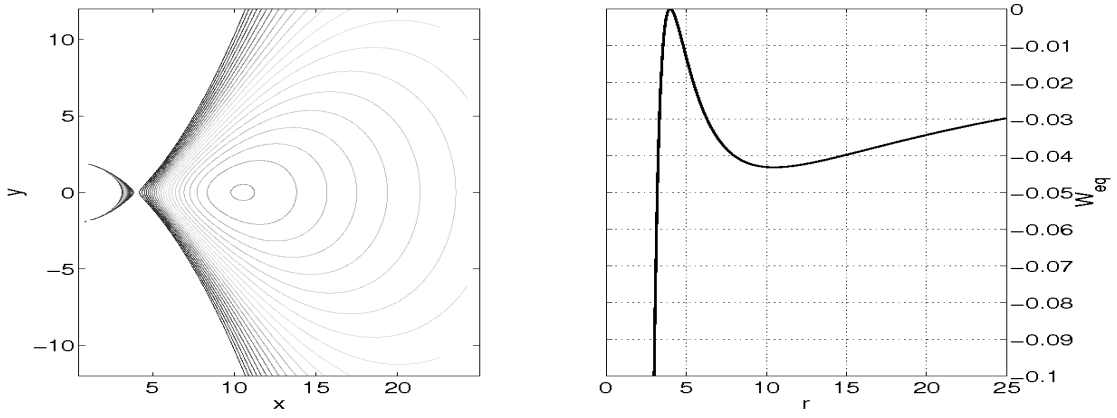

Figure 3.8: Equipotential surfaces and potential in the equatorial plane for $l = 4$

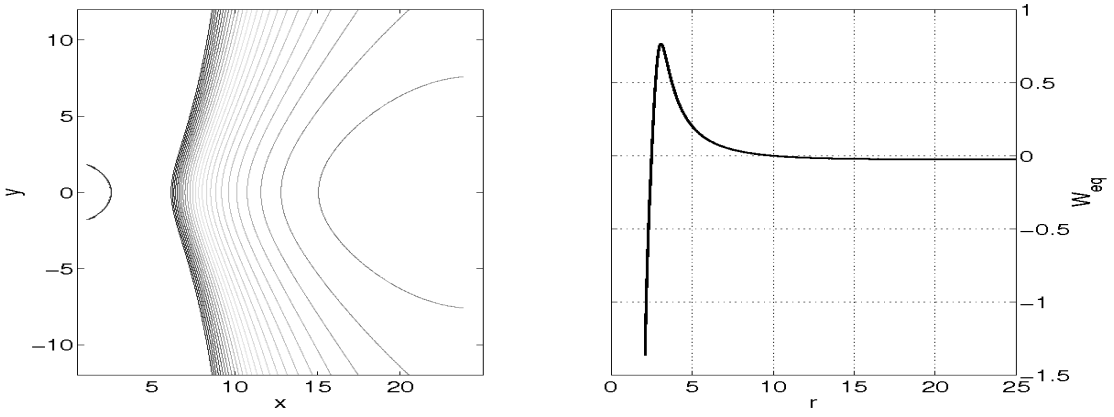

Figure 3.9: Equipotential surfaces and potential in the equatorial plane for $l = 5$

3.2.3 Equilibrium configurations with $l = Kr^{\alpha}$

Now we extend previous consideration to a power-law distribution of angular momentum:

$$l_{eq} = Kr^{\alpha} \tag{3.21}$$

where K and α are parameters of the configuration and axysymmetric space-time. The metric now reads:

$$ds^2 = -\frac{\Delta + a^2 sin^2\theta}{\varrho^2}dt^2 - 2a\frac{2M_{bh}rsin^2\theta}{\varrho^2}dtd\phi + \frac{\varrho^2}{\Delta}dr^2 + \varrho^2 d\theta^2 + \frac{\Sigma}{\varrho^2}sin^2\theta d\phi^2 \tag{3.22}$$

where

$$\Delta \equiv r^2 - 2M_{bh}r + a^2, \tag{3.23}$$

$$\varrho \equiv r^2 + a^2 cos^2\theta, \tag{3.24}$$

$$\Sigma \equiv (r^2 + a^2)^2 - a^2\Delta sin^2\theta. \tag{3.25}$$

Here we used standard Boyer-Lindquist coordinates and M_{bh} and a, respectively, are the mass and the angular momentum per unit inertial mass of the central object. In principle one can consider both prograde and retrograde orbits in which the disc is orbiting in the same or in the opposite direction of the central object but here we will restrict to corotating orbits (i.e. $l_{eq} > 0$ and $a > 0$). This restriction is based on the very scarce relevance that retrograde discs seem to have in astrophysical scenarios.

Also in this case the physical considerations about limits on the value of the angular momentum made for the case $l = const$ hold. Differences are that here we have a keplerian angular momentum (and thus all the limits based on it) that depends on a:

$$l_{K,eq} = \frac{r^2 - 2a\sqrt{r} + a^2}{(r-2)\sqrt{r} + a}, \tag{3.26}$$

and that the distribution of angular momentum has 2 parameters. Also in this case there are limiting values of the angular momentum to have a cusp and a center , but these will be limits on the constant K in the angular momentum law.

First of all we have a limit coming from the condition for the energy per unit inertial mass (3.16) to be real:

$$g_{tt}l^2 + 2g_{t\phi}l + g_{\phi\phi} > 0 \Rightarrow l < l_{cr} \tag{3.27}$$

with

$$l_{cr} = \frac{g_{t\phi} + \bar{\omega}}{-g_{tt}}. \tag{3.28}$$

This condition on the angular momentum becomes a condition on the constant K i.e. $K \leqslant K_{cr}$ where:

$$K_{cr} = \frac{l_{cr,eq}(r_{cr})}{r_{cr}^{\alpha}}, \tag{3.29}$$

and r_{cr} is the solution of:

$$\frac{dln(|l_{cr,eq}|)}{dln(r)}(r_{cr}) = \alpha. \tag{3.30}$$

Here we see how the exponent in the power law α and the angular momentum of the central object a come into play: depending on their values the equation above will have or not acceptable solutions.

- for $0 \leqslant \alpha < 1/2$ (sub-Keplerian discs) and $0 \leqslant a < 1$ there's only one root and it is outside the horizon. If $a = 1$ then this root goes in the horizon.
- for $1/2 \leqslant \alpha < 1$ (keplerian and super-keplerian discs) there's only one root outside the horizon, for all the values of a.
- for $\alpha = 1$ this root is pushed to infinity and thus $K_{cr} = 1$.
- for $\alpha = 1$ there's always a root and thus we don't consider this case.

The most interesting feature of the equilibrium configuration is the presence of the cusp and of the center. The existence of these points is determined by the geometry of the equipotentials, which in turn depend on the solutions of (3.17). In this case, similarly to the critical values discussed before, we have that the condition for equation (3.17) to have a solution, once tranferred to the constant K, becomes:

$$K \geqslant K_{ms} \tag{3.31}$$

where

$$K_{ms} = \frac{l_{K,eq}(r_{ms})}{r_{ms}^{\alpha}}, \tag{3.32}$$

and r_{ms} is the solution of:

$$\frac{dln(|l_{K,eq}|)}{dln(r)}(r_{ms}) = \alpha, \tag{3.33}$$

and again for the different values of alpha we have:

- for $0 \leqslant \alpha < 1/2$ the root r_{ms} is unique and finite.
- for $\alpha = 1/2$ the root goes to infinity ($K_{ms} = 1$).
- for $\alpha > 1/2$ there's no root.

It is worth stressing that the root of the equation (3.33) r_{ms} is not the radius of the cusp or of the center; these points are still the roots of equation (3.17). r_{ms} instead is the point where, given a and α, the cusp and the center are located for $K = K_{ms}$. For greater values of K the cusp will be located at $r < r_{ms}$ and the center at $r > r_{ms}$.

Finally, we want that the equipotential passing through the cusp to be closed, for accretion to be possible. This means that:

$$W_{eq}(r_{cusp}) = 0, \tag{3.34}$$

and thus that the constant K has to fullfill the condition:

$$K \leqslant K_{mb} \tag{3.35}$$

The value K_{mb} is determined solving equation (3.34) for K (W_{eq} depends on l, see(3.15)) at $r = r_{cusp}$.

For the keplerian and sub-keplerian cases we have $K_{cr} > K_{mb} \geqslant K_{ms} \geqslant 1$ and the cusp and the center of the disc are at the local maximum and minimum (if any) of the potential. If $\alpha > 1/2$ then the center is rejected to infinity and $K_{mb} = 0$.

3.2.4 The runaway instability

The first work about the runaway instability is the one by Abramowicz, Calvani and Nobili [6] in 1983. The idea was quite clear and simple: after all the works by many authors done in the previous years about the equilibrium configuration of accretion discs the picture was that of a system that had a structure similar to that of a close binary; in particular there were Roche lobes and lagrangian points as in the binary case. The attention was driven to the inner lagrangian point L_1 because if the disc would have filled his own lobe, then accretion on the black hole would have started, thus modifying the position of L_1 and possibly leading to the total disruption of the disc on a dynamical timescale. The work was based on some simplifying assumptions:

- pseudo-newtonian treatment of gravity
- constant angular momentum distribution inside the disc
- non rotating black hole
- approximate self-gravity of the disc

and gave as a result that the disc was unstable to the runaway instability. The problem of the stability of an accretion disc to such a process is an important one because of the number of astrophysical scenarios involving it, more, many of them require the disc to be stable on time scales much longer than the one of the instability (which is of the order of a few milliseconds). One tipical example of this models is the GRB: the observed electro-magnetic emission is the result of the interaction of the shocks present in a relativistic wind of particles. These shocks interact both between themselves and with the circumstellar media, causing all the tipical peaks that we observe in the luminosity. The model that explains all the features of the emission and that is the standard scenario for GRB's, the "fireball shock model" [50], is based on the existence of a central engine that powers the

relativistic wind of particles. The nature of this central engine is still matter of debate and many hypotheses have been formulated. The most promising one has an accretion disc as a key ingredient, providing matter to be accreted and thus energy to be extracted and funneled along the rotation axis by the magnetic field of the central object. It is clear that if an accretion disc has to be the engine of a GRB it has to live at least as long as the typical timescale for the phenomenon that is of the order of seconds. This timescale is much longer that the runaway instability one and this fact makes the stability issue a critical one: if the disc is disrupted after only a few milliseconds it cannot be the central engine of anything that lasts for seconds! Various studies over the years [80, 39, 57, 24, 7, 49, 47] have improved the treatment of the aspects mentioned before (a complete picture is synthetized in [29]) but were never capable to give a definitive answer to the runaway instability problem leading to alternate and contradictory results. The last work by A.Font and F.Daigne [23], which is the state of the art about runaway instability, was considering non self-gravitating discs, with a power-law distribution of angular momentum in the equatorial plane, the evolution of metric was mimicked by a sequence of stationary configurations with changing mass and angular momentum parameters, starting from a spherically simmetric initial data. The evolution of the parameters was done computing the mass and angular momentum flow through the event horizon. The result in this setup is that there is a critical value of the exponent $\alpha_c \backsim 0.05$ (depending sligthly on the disc model) in the angular momentum law above which the disc is stable.

Chapter 4

Barmode instability of differentially rotating neutron stars with realistic equation of state

In this chapter we describe all the results of simulations done with realistic equations of state. First, in section 4.1 we describe the equilibrium configuration obtained with our initial model code, emphasizing on the differences between realistic and polytropic eos, then section 4.2 is about the preliminary runs done with spherically simmetric stars that let us show the consequence of using an unconsistent fit (i.e. the HP one). In section 4.4 there are then the results for rotating models. These results are partly obtained with the techniques described in section 4.3.

4.1 Initial data

The initial data are generated with the RNS code by Stergioulas [76], modified to include realistic equations of state. This code solves the Einstein's equations coupled to matter described in [40] in axysymmetry and accepts as input the central density of the star ρ_c and the ratio between polar and equatorial radii $a = r_p/r_e$. The metric is assumed to be thus the general axysymmetric metric:

$$ds^2 = -e^{\mu+\nu}dt^2 + e^{\mu-\nu}r^2 sin^2\theta(d\phi - \omega dt)^2 + e^{2\xi}(dr^2 + r^2 d\theta^2) \qquad (4.1)$$

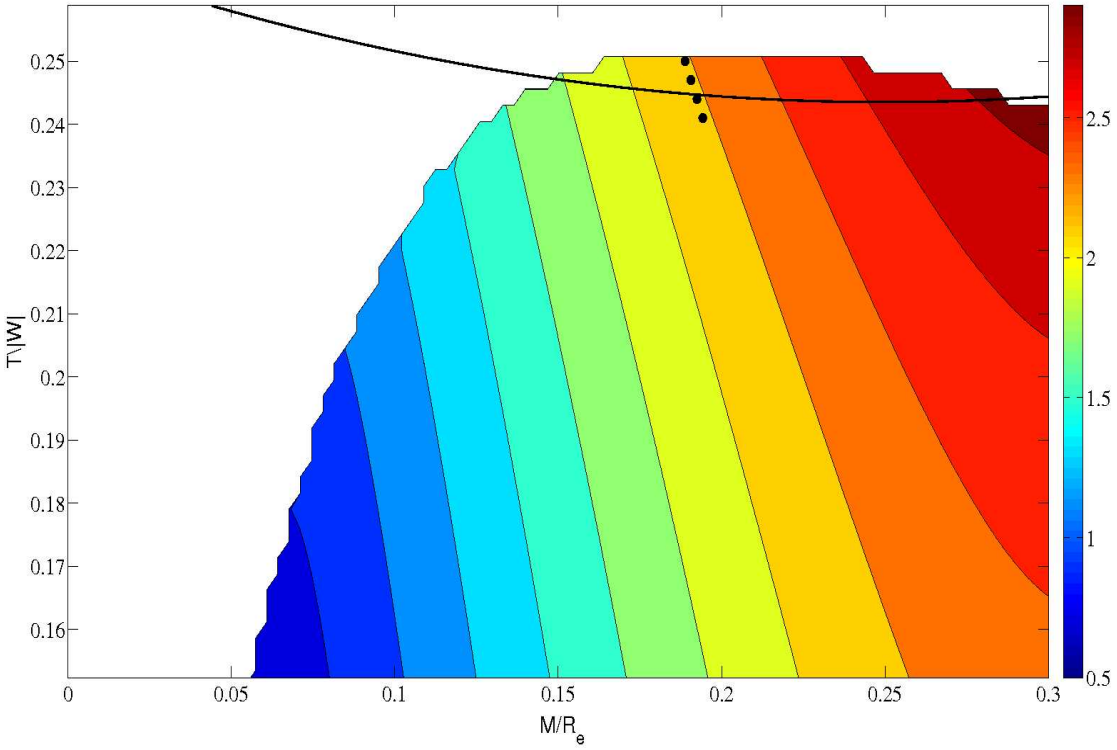

Figure 4.1: β-compactness plane for initial models computed with SLy EOS. The four black dots mark the models in table 4.1 that we choose for evolution. Color scale indicates the gravitational mass. The black curve is the stability curve for polytropic EOS

where μ, ν, ξ and ω are space-dependent metric functions. This code generates the initial data once supplied with an equation of state and a rotation law. In our case the rotation law is the standard differential rotation law used in neutron star studies:

$$\Omega_c - \Omega = \frac{r_e^2}{\hat{A}^2}\left[\frac{(\Omega-\omega)r^2 sin^2\theta e^{-2\nu}}{1-(\Omega-\omega)^2 r^2 sin^2\theta e^{-2\nu}}\right] \tag{4.2}$$

where r_e is the coordinate equatorial radius of the star and the coefficient $\hat{A}$ is a parameter controlling the degree of differential rotation. We set $\hat{A} = 1$ in analogy with other works in literature. As equation of state we used the HP fit done on the SLy table described in section 3.1.1.

We generated a big number of initial models and show the result in figure 4.1 on a compactness-β plane. For comparison we show the correspondig results computed with a polytropic EOS in figure 4.2. It is also shown in both figures

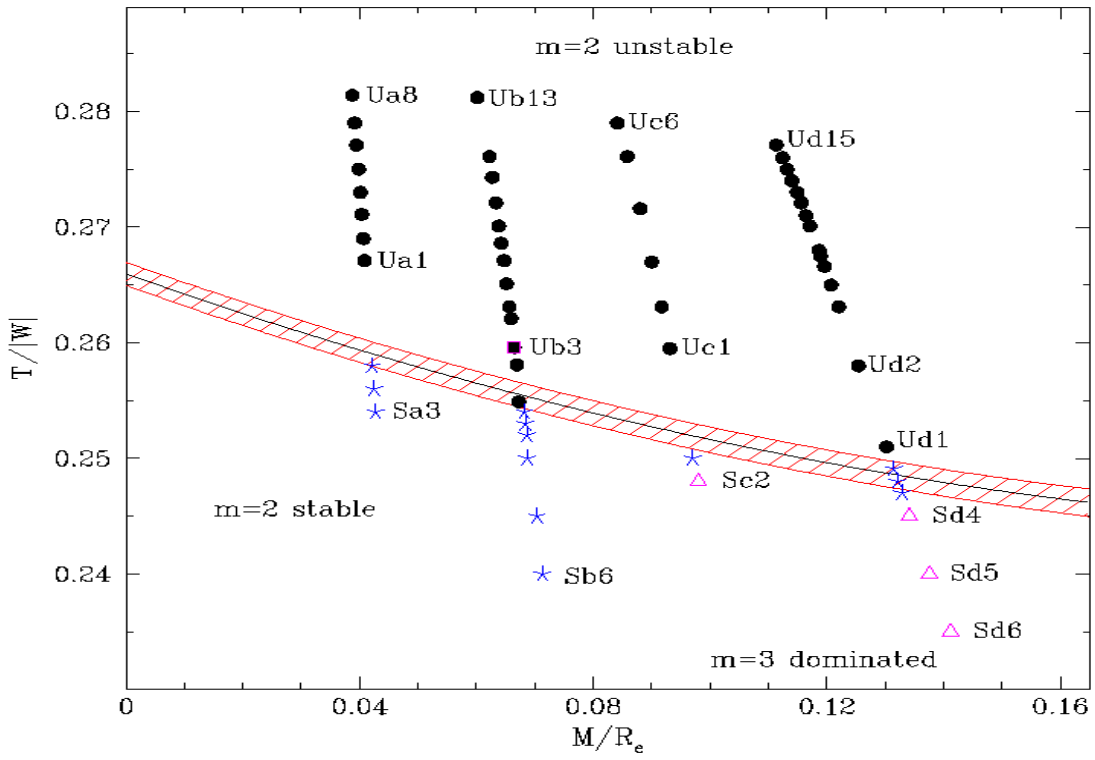

Figure 4.2: β-compactness plane for initial models computed with polytropic EOS. Dots mark models studied in [48].The black curve, which is reported also in figure 4.1 divides stable and unstable models

the stability curve determined in [48] for polytropic EOS. Comparing the two it is clear that using a realistic EOS it is possible to generate much more compact models with respect to the polytropic ones ($M/R = 0.3$ was not reachable with the polytropic) and, at the same time, high values of β that were reachable with the polytropic EOS, now are not.

We choose for the evolution 4 models on a $M_{barionic} = 2.5 M_{sun}$ sequence to probe a part of the parameter space in which we expect the instability to develop, in particular we choose 4 models across the stability curve for polytropic EOS so to test immediately if the critical value of β for SLy EOS was close to the value computed for the polytropic EOS. These models are shown with black dots in figure 4.1. The details of the four models are summarized in table 4.1 and in figure 4.3 we plot the density and angular velocity contours at $t = 0$.

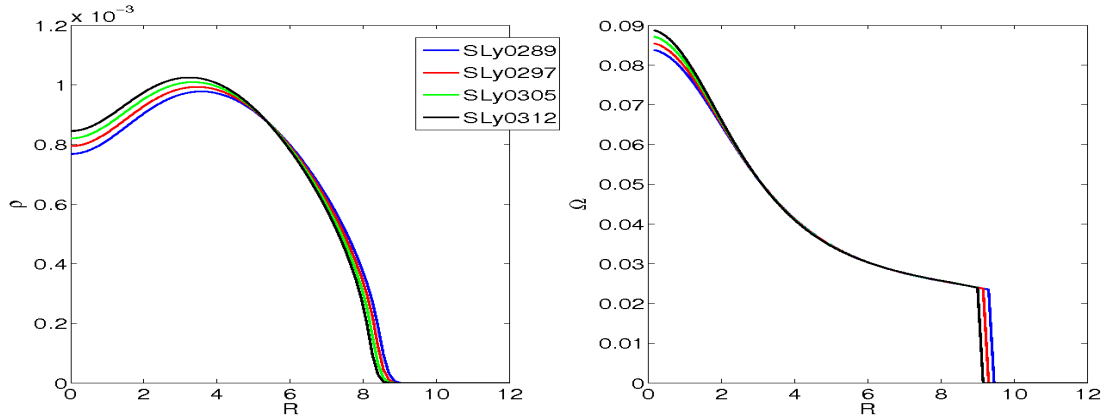

Figure 4.3: Profiles of the density and of the angular velocity for models in table 4.1

Model	β	M/R	r_e	r_p/r_e	τ_D (msec)	ν_0 (kHz)	ν_1 (kHz)	$\frac{\nu_0}{\nu_1}$
SLy0289	0.250	0.206	12.08	0.289	3.80	2.225	3.489	0.63
SLy0297	0.247	0.209	11.95	0.297	5.96	2.258	3.590	0.62
SLy0305	0.244	0.211	11.82	0.305	6.54	2.324	3.648	0.64
SLy0312	0.241	0.213	11.70	0.312	9.91	2.422	3.803	0.64

Table 4.1: Values of instability parameter β, compactness, equatorial radius, axes ratio for the initial data and bar duration, frequency of the main and of the second peak and ratio between the two for each evolution (see figures 4.6-4.9

4.2 Time evolution of non rotating stars with realistic cold EOS

As a code test we first used a spherically symmetric star (see table 4.2 for details) with 3 different grid resolutions ($\Delta x = 0.2, 0.15, 0.1$). The grid structure details for the three runs are in table 4.3. All the runs are in octant symmetry and no perturbation is added to the initial model so that the oscillations are triggered only by the truncation error. The equation of state used was the HP cold fit described in section 3.1.1. The analysis of the evolution of the central density gave an unexpected outcome: instead of the expected convergence behaviour the amplitude of the oscillations of the central density was increasing with the resolution as is

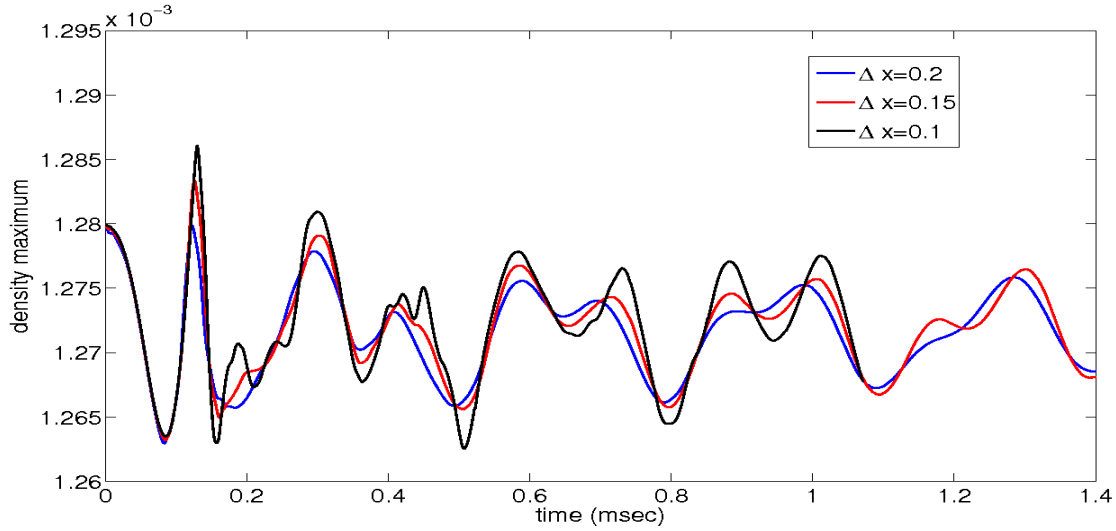

Figure 4.4: Anticonvergence of oscillations of the maximum of the density for model Sly10

model	ρ_c	mass	radius	eos
SLy10	1.28×10^{-3}	1.17	6.8	HP

Table 4.2: Parameters for the initial model

shown in figure 4.4.

We explored a number of possible causes for this anticonvergence that can be summarized with: accuracy of the initial model, effect of the grid structure (refinement boundaries too close to the star). The reason of the anticonvergence, in the end, turned out to be the thermodynamic inconsistency of the used fit.

To avoid this inconsistency we changed the expression (3.2) we used to compute the pressure

$$\begin{aligned}\zeta = &\frac{a_1 + a_2\xi + a_3\xi^3}{1 + a_4\xi} f_0(a_5(\xi - a_6)) + \\ &+ (a_7 + a_8\xi) f_0(a_9(a_{10} - \xi)) + \\ &+ (a_{11} + a_{12}\xi) f_0(a_{13}(a_{14} - \xi)) + \\ &+ (a_{15} + a_{16}\xi) f_0(a_{17}(a_{18} - \xi))\end{aligned}$$

(remember $\xi = log(e)$, $\zeta = log(p)$) with the expression (3.7)

$$p = \rho^2 \frac{d\epsilon}{d\rho}$$

Δx of finest level	number of refinements	refinement boundaries
0.2	3	[12M 20M 40M]
0.15	3	[9M 18M 60M]
0.1	4	[8.8M 16M 28M 60M]

Table 4.3: Details of the grid for the runs

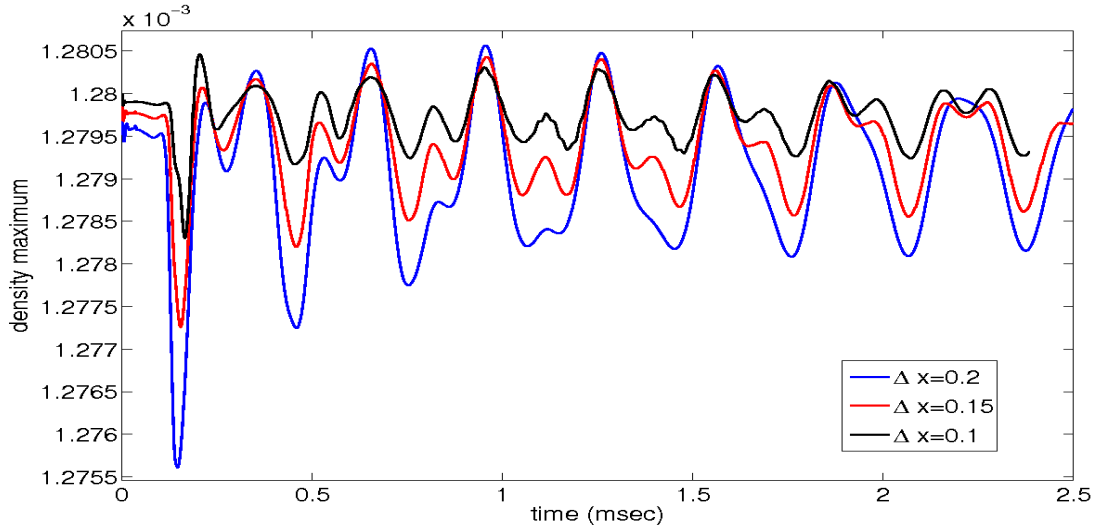

Figure 4.5: Maximum of the density for model SLy10 after modification to HP fit

used in the Shibata fit that comes directly from the first principle of thermodynamics. The results with this new expression for the pressure are in figure 4.5. The radial oscillation frequency of 3.129 kHz ectracted from our 3D data is in good agreement with the frequency extracted with the 1D perturbative code PerBACCo (courtesy of Sebastiano Bernuzzi, [11]) of 3.085 kHz with a relative difference of 1.4%. This agreement is a good test of the reliability both of the Whisky code and of the implementation of the EOS that we made.

4.3 Analysis technique

For the four initial models considered we follow the evolution of various quantities, following the approach in [14] to let the results be comparable. We briefly list and comment on these quantities and on their relevance for our analysis:

- quadrupole moment of the matter distribution:

$$I^{ij} = \int d^3x D x^i x^j \tag{4.3}$$

This choice is dictated by the fact that the density D is a conserved quantity in the evolution scheme that we use, other choices with the same Newtonian limit would have been the rest-mass density ρ or the T_{00} component of the energy-momentum tensor.

- distortion parameters: from the quadrupole moment we can compute 2 different distortion parameters:

$$\eta_+ = \frac{I^{xx} - I^{yy}}{I^{xx} + I^{yy}} \tag{4.4}$$

$$\eta_\times = \frac{2I^{xy}}{I^{xx} + I^{yy}} \tag{4.5}$$

$$\eta = \sqrt{\eta_+^2 + \eta_\times^2} \tag{4.6}$$

These quantities are useful to quantify the size and the presence of a bar.

- hydro modes: to really understand the evolution of the star and of the instability we decopose the rest-mass density in Fourier modes so that the "power" or the m-th mode is:

$$P_m \equiv \int d^3x \rho e^{im\phi} \tag{4.7}$$

and the "phase" of the m-th mode is defined as:

$$\phi \equiv arg\left(P_m\right). \tag{4.8}$$

This analysis, done in post-processing, is the main one in our study since it permits to define various stages of the evolution in which the star is dominated by a different deformation type and so to determine the duration of the bar deformation. Besides this it is possible to state whether the dynamics is fully non linear or it can also approximated by a linear treatment.

- center of mass: given that we do not impose any symmetry other than a reflection on the x-y plane the center of mass is free to move in this plane. We therefore monitor the position of it through:

$$X^i_{cm} = \frac{1}{\tilde{M}} \int d^3x \rho x \tag{4.9}$$

where $\tilde{M} = \int d^3x\rho$. The main reason to do this is that it has been observed a drift of the star at late times due to numerical errors that was only possible to shift in time enlarging the grid size, so checking when the star goes off the first grid cell we have a limit to the duration of our simulations.

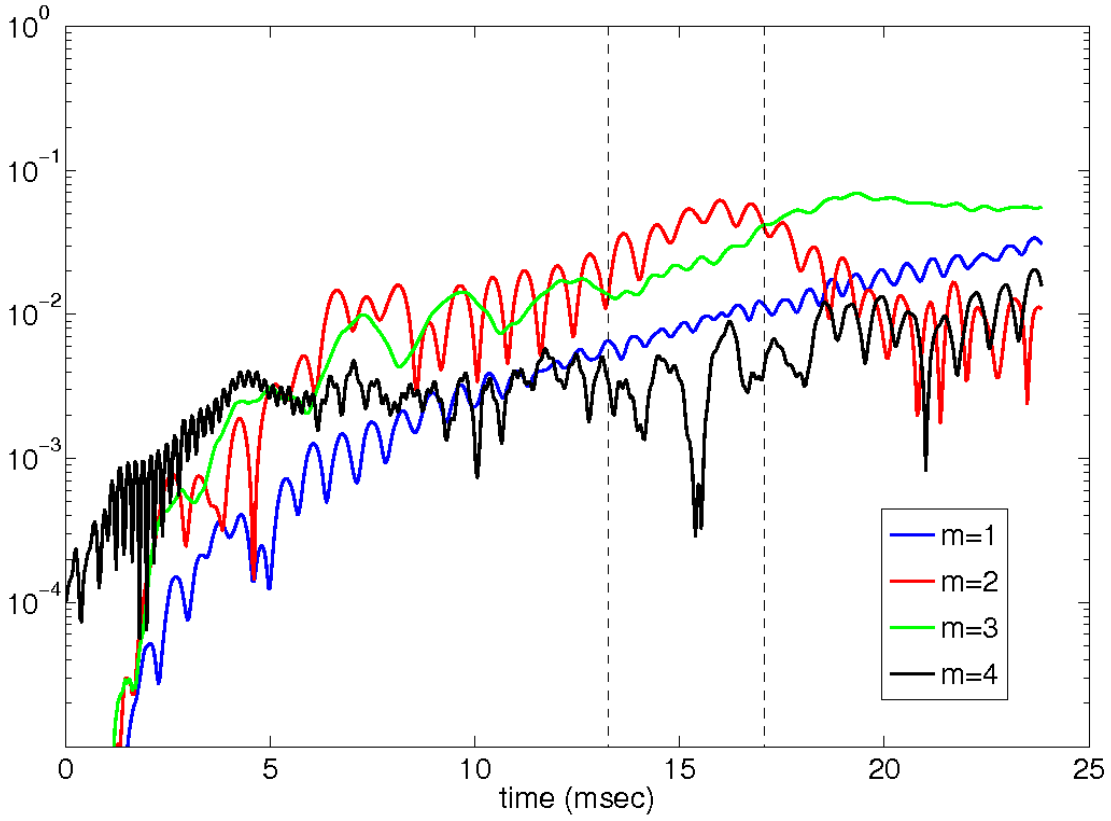

Figure 4.6: Time evolution of $m = 1, 2, 3, 4$ modes computed with expression 4.7 for model SLy0289. Between the two vertical dashed lines the $m = 2$ mode is dominant.

4.4 Results for rotating models

Here we present the detailed results of the runs for our four models. All the four simulations were made with a resolution $\Delta x = 0.15$ on a grid with 3 refinement levels with outer boundaries placed at $60M$. From these results there are a number of things that can be stated but on many questions we still can't give a definite

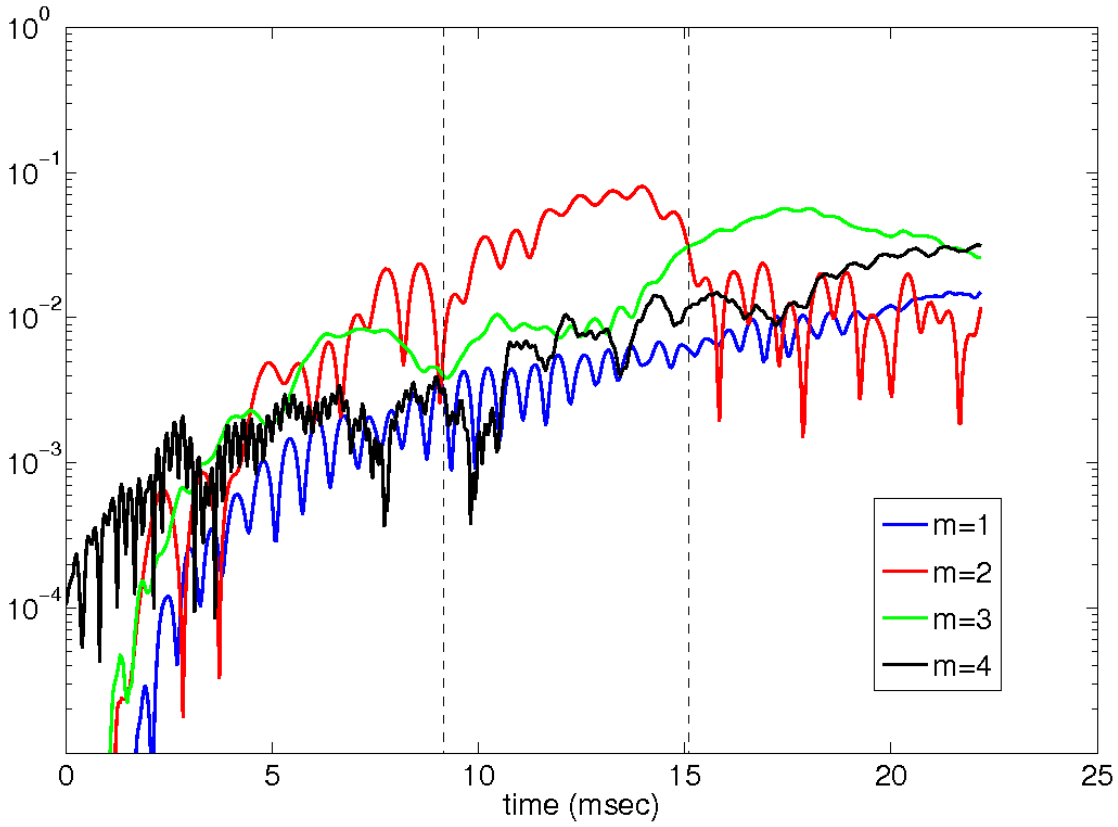

Figure 4.7: Time evolution of $m = 1, 2, 3, 4$ modes computed with expression 4.7 for model SLy0297. Between the two vertical dashed lines the $m = 2$ mode is dominant.

answer. First of all we can find a general behaviour in all of the four models, with little deviations. What we see is that there are common phases between models in which the same mode evolve in the same way (see figures 4.6-4.9 where we show the time evolution of th $m = 1, 2, 3, 4$ modes, computed with expression 4.7, for each model). Going into details we can define 5 phases:

- a first phase in which the dominant mode is the grid deformation $m = 4$. In this phase the $m = 2$ and $m = 3$ modes grow till they reach the $m = 4$. The $m = 1$ mode, though growing is the lowest of the four.
- after the $m = 2$ and $m = 3$ modes have crossed $m = 4$ they continue to grow, keeping comparable values probably due to numerical noise.
- the $m = 2$ begins to grow and becomes the dominant one.

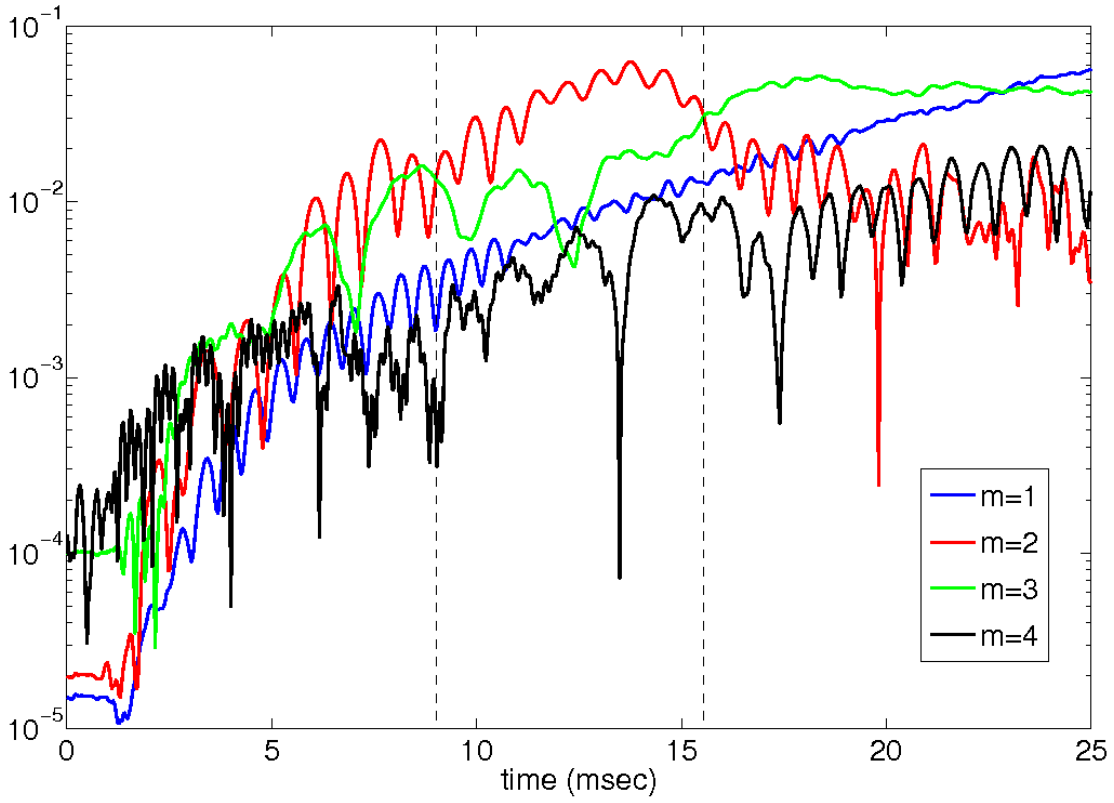

Figure 4.8: Time evolution of $m = 1, 2, 3, 4$ modes computed with expression 4.7 for model SLy0305. Between the two vertical dashed lines the $m = 2$ mode is dominant.

- after the $m = 2$ mode has decreased the $m = 3$ mode experiences a growth similar to the one in the $m = 2$ mode and becomes in turn the dominant one.

- the $m = 3$ mode decreases in amplitude leaving the $m = 1$ or $m = 4$ as the dominant mode.

Some points of these qualitative analysis must be discussed to understand what is really different from the polytropic case and what is not. The main issue is whether these four models are unstable or not, we do clearly see a growth in the $m = 2$ mode but this growth is not exponential as it should be for really unstable models thus we can conclude that ther is only a non clear evidence for bar-mode instability in these models. Besides being due to the realistic EOS we use, there's another

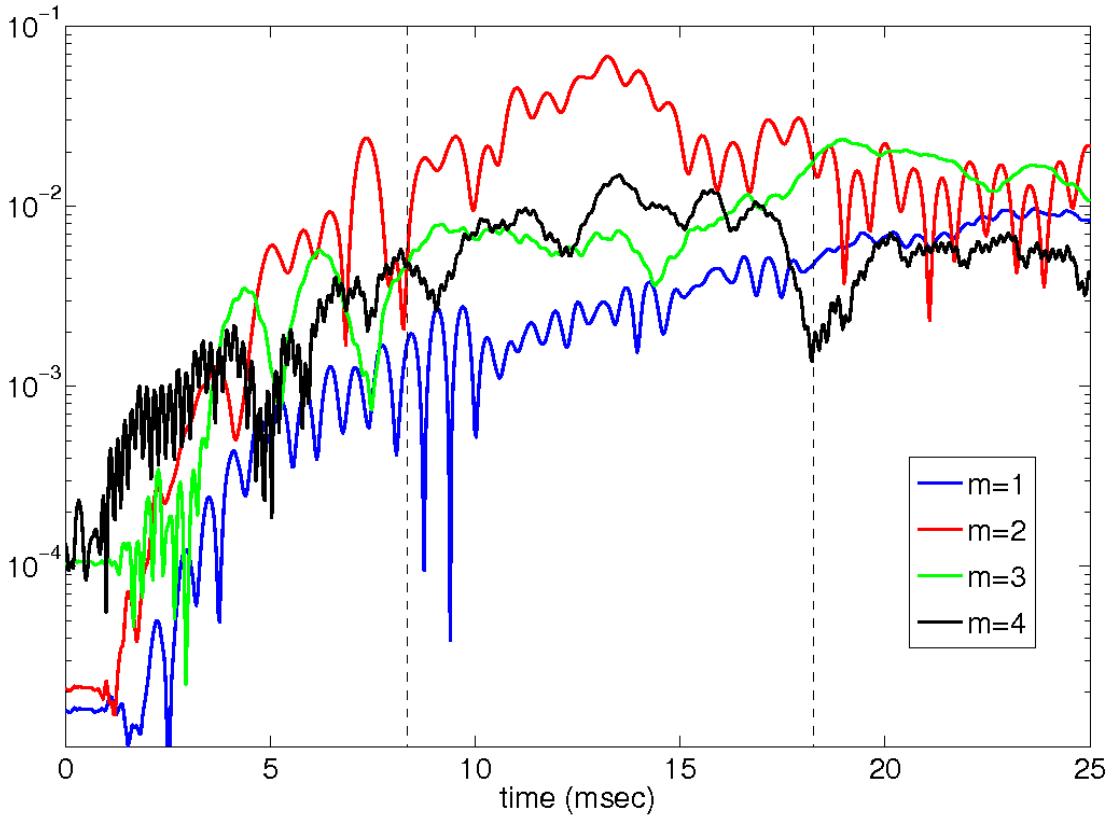

Figure 4.9: Time evolution of $m = 1, 2, 3, 4$ modes computed with expression 4.7 for model SLy0312. Between the two vertical dashed lines the $m = 2$ mode is dominant.

possibility: the models could be very close to the threshold. A similar behaviour has been seen in polytropic stars for which models near the threshold showed non clearly exponential growth of the $m = 2$ mode. This aspect has to be investigated further by exploring a wider portion of parameter space. The fact that we are able to generate initial models with β only slightly over the threshold for the onset of the instability for polytropic EOS is a limit at present for this investigation. Also the fact that the dominant mode in the last phase of the evolution is not always the same is an indication that we could be close to the threshold and drives us to say that we still can't draw any definitive conclusion about the threshold for the onset of the instability. To clarify the appearence of the various modes in these stages of the evolution we show in sections 4.4.1-4.4.4 snapshots of the rest mass density in the equatorial plane from the evolutions at these times:

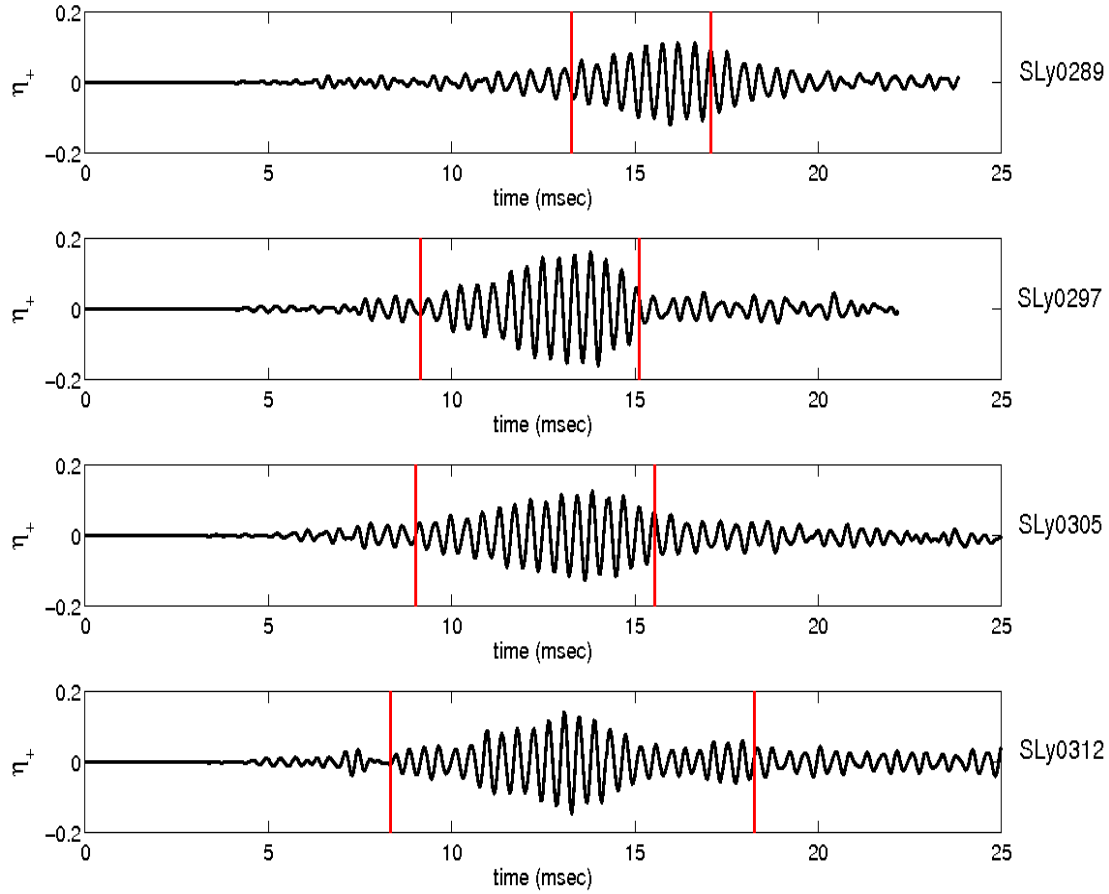

Figure 4.10: Time evolution of the η_+ for the four models, the red vertical lines indicate the period during which the $m = 2$ mode is dominant

- $m = 4$ gets crossed by the $m = 2$ and $m = 3$
- $m = 2$ becomes the dominant mode
- $m = 2$ reaches the maximum value
- $m = 3$ reaches the maximum value

It is worth stressing how the matter configurations at each of these steps are similar to each other but the time at which they are present are different among models.

Besides these qualitative features there are anyway some quantitative information that can be extracted from these data. First of all it is clear from figure 4.10 that the maximum value attained by the deformation parameter η_+, computed

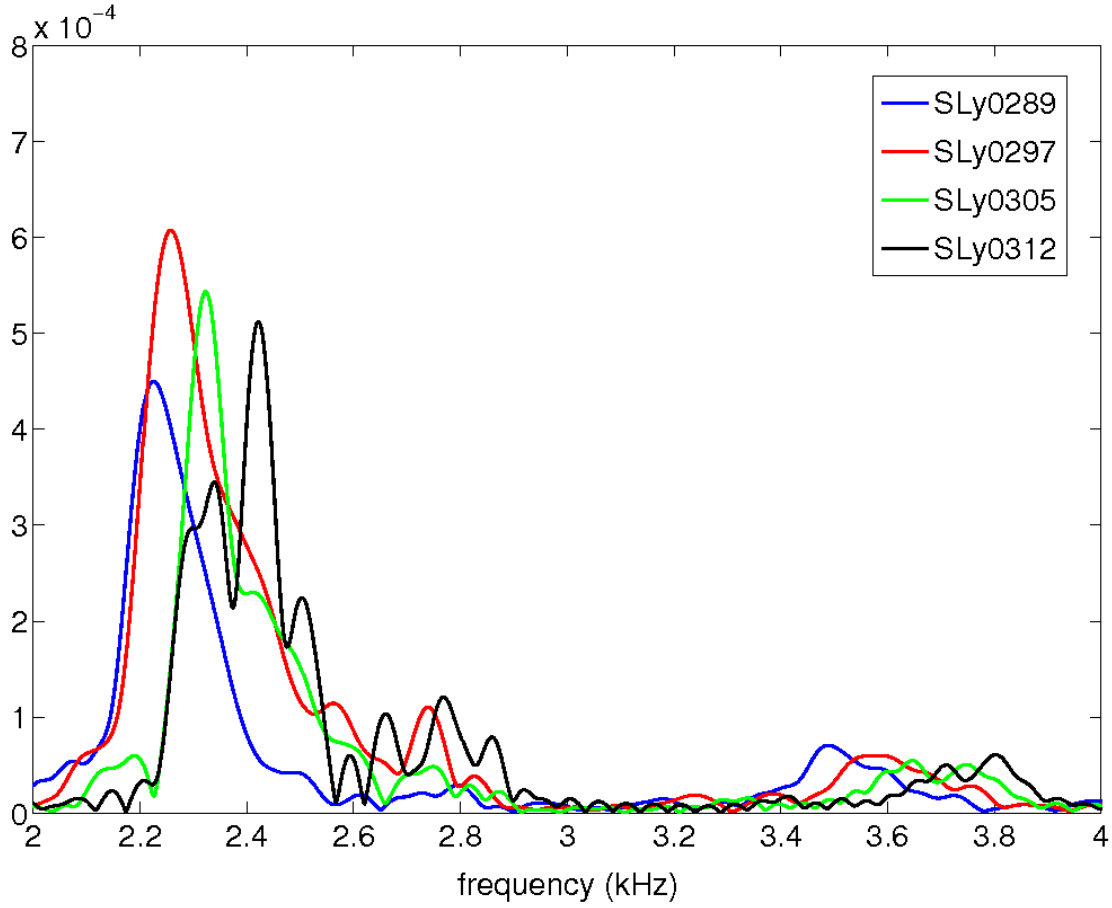

Figure 4.11: Fourier spectra of the four models. Peak frequency can be found in table 4.1

with expression 4.4 is much lower ($\backsim$ 5 times) than the maximum of $\eta_+ \backsim 0.7$ reached with the polytropic. Consequence of this minor deformation is the fact that the spiral arms, though present, are very thin. Actually they are not visible when visualizing data in a linear scale, so we show, as an example, the snapshot taken from the evolution of model SLy0305 when the $m = 2$ and the $m = 3$ reach their maximum also in logaritmic scale (figures 4.12-4.13). With this scale the spiral arms are evident and distinct from each other, even in figure 4.13 where there are three visible. From the time series for η_+ we can also extract information about the spectrum from figure 4.11 where we can see that besides the main peak at around 2.3 kHz it is clearly visible the peak at 3.6 kHz that is due to the $m = 3$ deformation.

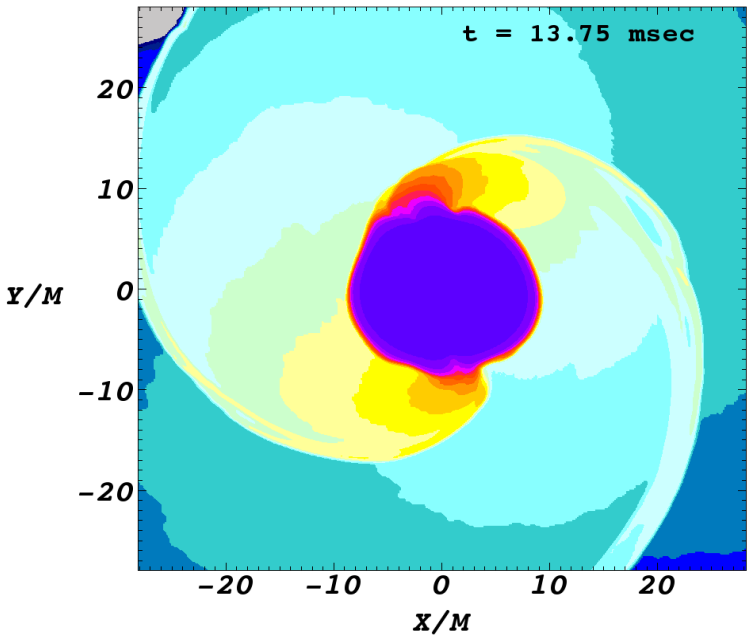

Figure 4.12: Rest mass density in the equatorial plane for model SLy0305 at the moment of maximum value of the $m = 2$ mode, in logarithmic scale

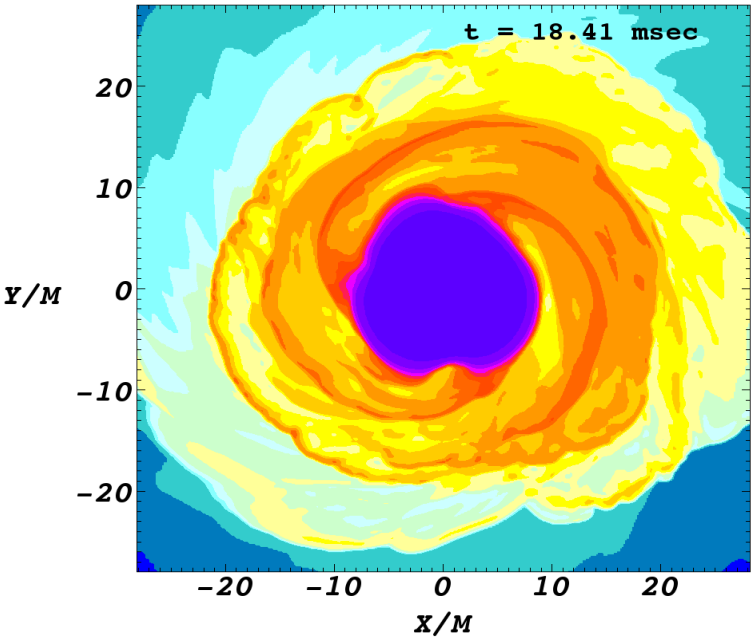

Figure 4.13: Rest mass density in the equatorial plane for model SLy0305 at the moment of maximum value of the $m = 3$ mode, in logarithmic scale

Another aspect which can be discussed here to compare polytropic and realistic EOS is the duration of the bar deformation. This quantity τ_D is defined as the time during which the $m = 2$ mode is the dominant one and the values for our models, reported in table 4.1, are muche less than those in [14]. The bar duration is marked in figures 4.6-4.9 with vertical lines at the times when the $m = 2$ becomes dominant and at the time when it gets overtaken by the $m = 3$.

In the following we show the snapsohts of the rest mass density distribution in the equatorial plane for all the 4 models at the times specified before.

4.4.1 Snapshots for model SLy0289

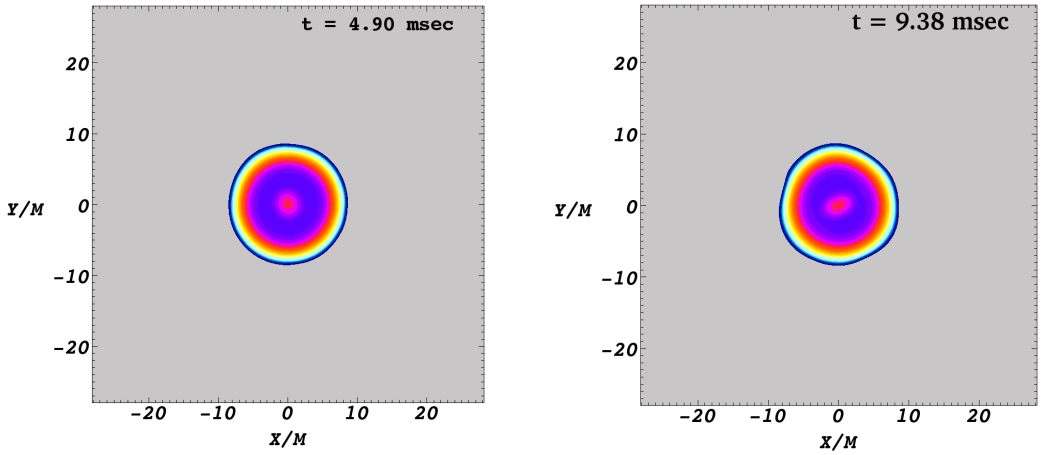

Figure 4.14: Snapshots of the rest mass density in the equatorial plane at $t = 4.90$ msec (left) and $t = 9.38$ msec (right)

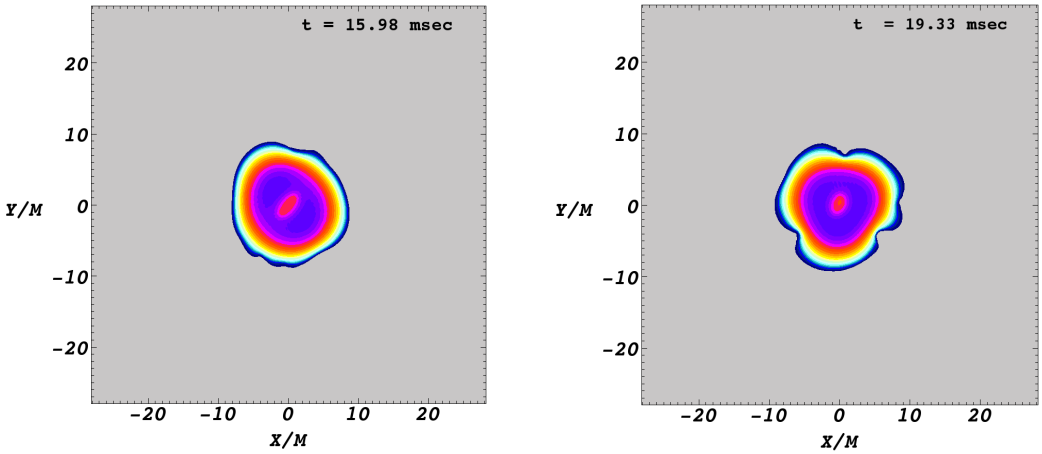

Figure 4.15: Snapshots of the rest mass density in the equatorial plane at $t = 15.98$ msec (left) and $t = 19.33$ msec (right)

4.4.2 Snapshots for model SLy0297

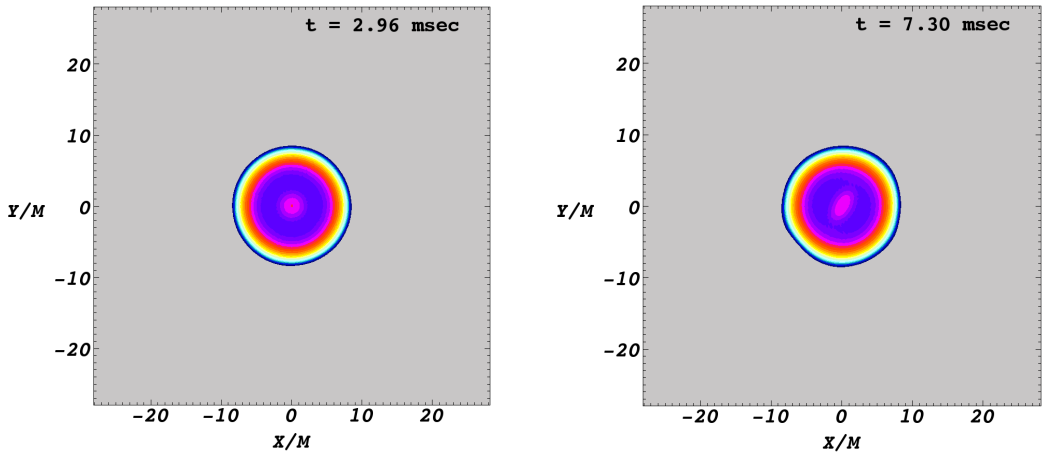

Figure 4.16: Snapshots of the rest mass density in the equatorial plane at $t = 2.96$ msec (left) and $t = 7.30$ msec (right)

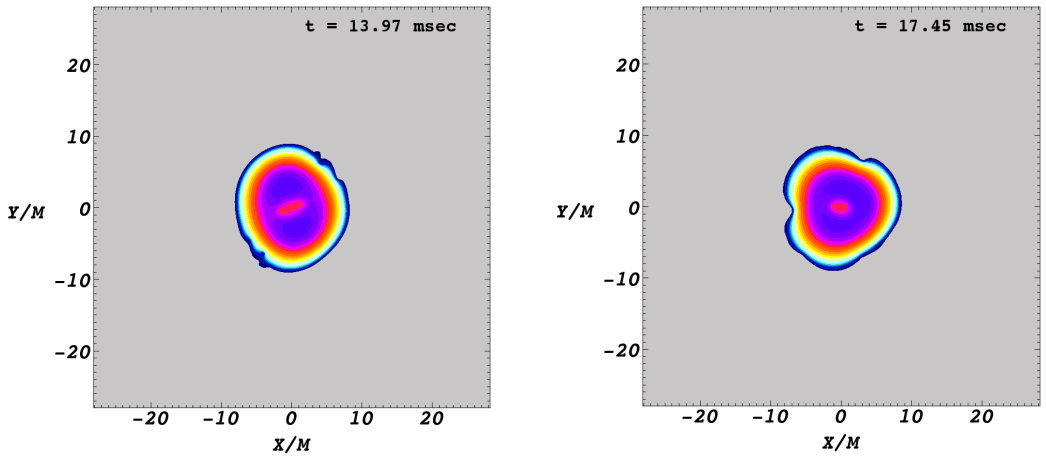

Figure 4.17: Snapshots of the rest mass density in the equatorial plane at $t = 13.97$ msec (left) and $t = 17.45$ msec (right)

4.4.3 Snapshots for model SLy0305

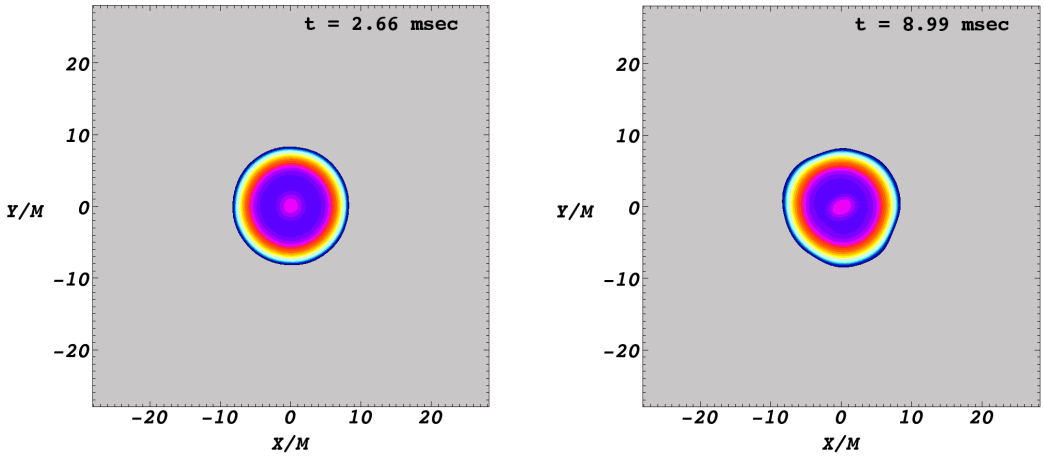

Figure 4.18: Snapshots of the rest mass density in the equatorial plane at $t = 2.66$ msec (left) and $t = 8.99$ msec (right)

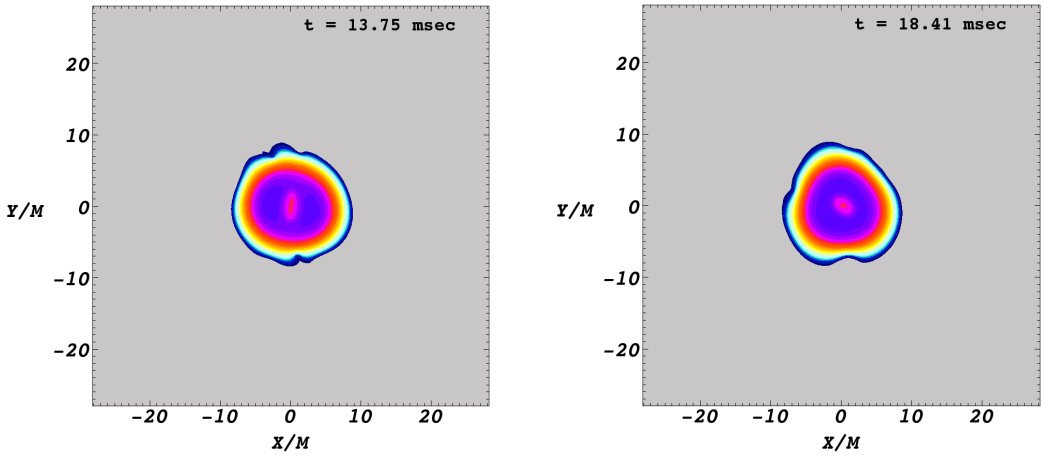

Figure 4.19: Snapshots of the rest mass density in the equatorial plane at $t = 13.75$ msec (left) and $t = 18.41$ msec (right)

4.4.4 Snapshots for model SLy0312

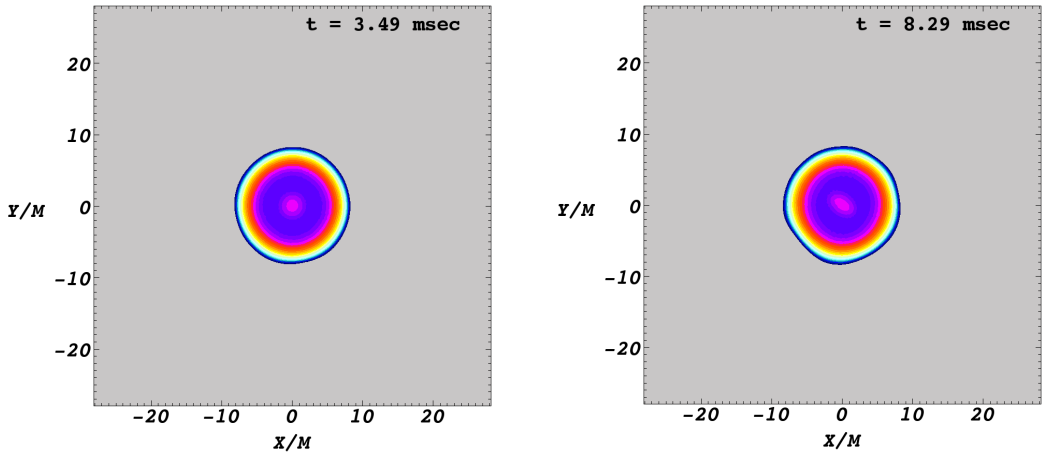

Figure 4.20: Snapshots of the rest mass density in the equatorial plane at $t = 3.49$ msec (left) and $t = 8.29$ msec (right)

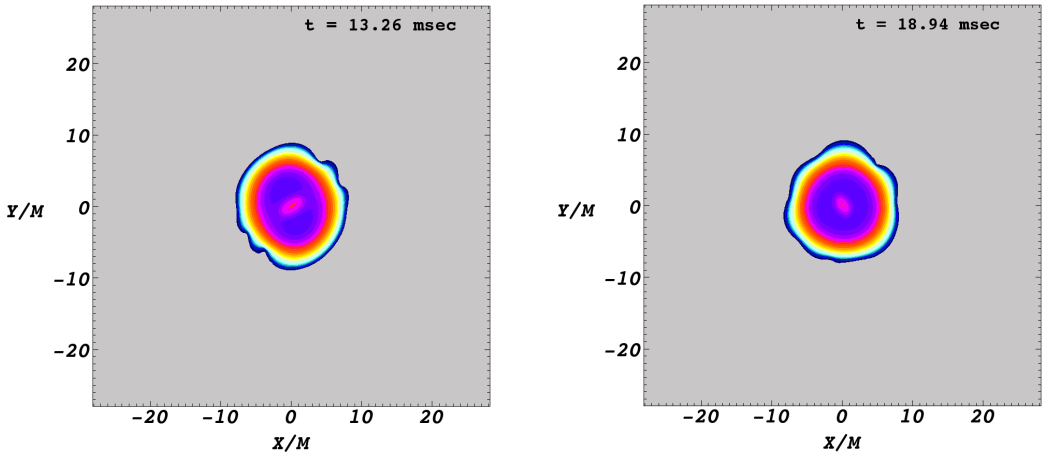

Figure 4.21: Snapshots of the rest mass density in the equatorial plane at $t = 13.26$ msec (left) and $t = 18.94$ msec (right)

Chapter 5

Accretion discs around spherically simmetric neutron stars

In this chapter we discuss the result of the runs for accretion discs aroud TOV stars. The physical problem that we want to address is the accretion driven collapse described in the introduction of a neutron star to a black hole. To do this we use the code TORERO to generate as initial data an unstable disc so that the accretion is triggered. We follow then the evolution of the mass flow an the central star and the evolution of the velocity inside the star due to the dragging of the orbiting infalling matter. The first section is dedicated to the description of the code TORERO and of the algorithm it implements to generate initial data, then in section 5.2 we discuss the capability of the evolution code to keep the system stable in different scenarios and in section 5.3 we discuss the evolution of the system.

5.1 Initial data

The initial data for the runs are generated with the code TORERO. This code is meant to generate discs in a stable, marginally stable or unstable configuration. It handles axisymmetric spacetimes and angular momentum power law in the equatorial plane. The self gravity of the disc is neglected. It is written in $c = G = 1$ units, the mass unit is the mass of the central object, we will call these units "central object units" (COU).

5.1.1 Algorithm

The algorithm that is at the basis of the TORERO code is the one described in [23]. Basically it is an algorithm to find the correct value of the angular momentum constant K for which the mass of the disc is the required one. Here we describe it some detail and explain its limits. The code accepts 7 physical and 3 numerical parameters:

- mass of the black hole M_{BH}
- spin of the black hole a
- mass of the disc in COU M_D
- depth level reached by the disc inside the potential well δ: the potential gap is determined as:

$$\Delta W \equiv W_{in} - W_{cusp} = \delta \times (W_{cusp} - W_{centre})$$

- exponent of the power law for the angular momentum α
- polytropic exponent of the EoS Γ
- polytropic constant κ

plus 3 parameters that determine the structure of the grid and that I will describe later. The present version of TORERO is restricted to $\Gamma = 2$. The algortihm follows these steps:

1. from the values of a and α compute K_{cr} and K_{ms}
2. bisect between these values to find K_{mb}. At eache step of the bisection the radius of the cusp r_{cusp} and the potential $W(r_{cusp})$ are computed till convergence to the value of K for which $W(r_{cusp}) = 0$.
3. bisect again between K_{ms} and K_{mb} to find the value of K that we need. At each step of this bisection the mass of the disc is computed from

$$M_D = 2\pi \iint_{\rho>0} \frac{g_{\phi\phi} - g_{tt}l^2}{g_{\phi\phi} + 2g_{t\phi}l + g_{tt}l^2} (\rho h + 2p) \left(r^2 + a^2 cos^2(\theta)\right) sin(\theta) dr d\theta \tag{5.1}$$

using the thermodynamic parameters Γ and κ, ΔW and the mass of the black hole. In detail the steps to compute the mass are:

- given the value of K compute the position of the cusp and of the center and the value of the potential at these points
- compute the inner and outer radii of the disc through:

$$W_{in} = W_{cusp} + \Delta W \tag{5.2}$$

- adapt the numerical grid to the extension of the disc and compute the mass.

5.1.2 The computing grid

The grid setup is determined by 3 parameters: DEF_R, DEF_TH, EST_TH. There are DEF_R+1 equidistant points along th radial direction that cover the space from $r = r_{in} - 0.01$ to $r = r_{out} + 2$. In this way the distance between neighbouring points is:

$$dr = \frac{r_{out} - r_{in} + 2.01}{DEF\_R} \tag{5.3}$$

Along the θ direction instead there are DEF_TH equidistant point that cover a region of space that is determined by EST_TH in this way: the upper limit is at $\pi/2 + (\pi/10)\cdot$EST_TH and the lower at $\pi/2 - (\pi/10)\cdot$EST_TH. This feature was introduced to save computational time because the disc will never cover the whole θ domain from 0 to π.

5.1.3 Limits of the code and tests

As pointed out in the previous chapter only corotation is implemented. Numerical limits exist on the values of a and α that the code is able to handle, namely the models that TORERO is able to generate are restricted to:

- $\alpha \leqslant 0.4$
- $a \leqslant 0.98$

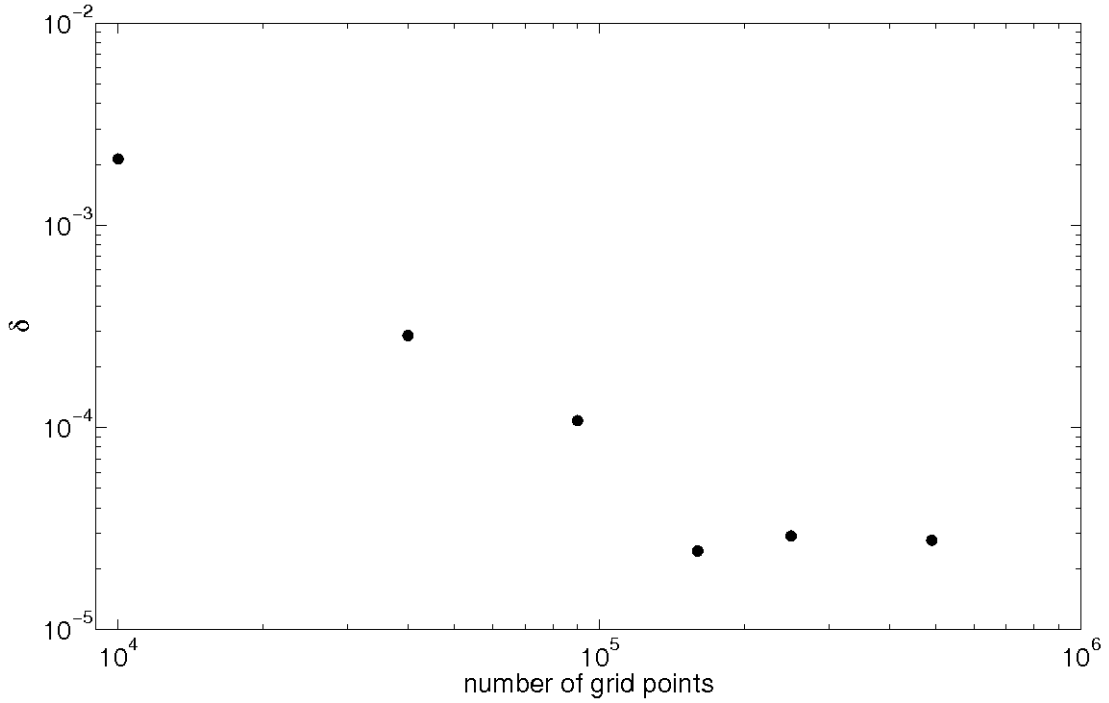

Figure 5.1: Convegence for disc mass computation

Within these limits all the routines have been tested for convergence and the overall result for convergence of the whole code is in figure 5.1. There we plot the relative difference between the requested (in this case 0.01 in COU) and the computed value of the mass of the disc versus the number of grid points. The quantity δm in figure is defined as:

$$\delta m = \left| \frac{(computed\ mass) - 0.01}{0.01} \right| \tag{5.4}$$

5.2 Stability runs and numerical setup

The evolution is performed with the 2D version of the Whisky code [38]. This code performs axysimmetric evolutions of the x-z plane, with staggered grid in the x direction. For the stability runs the outer boundary has been placed at $20M$ (except for the highest resolution run that has the boundary at $21M$ for grid consistency). The values of the hydrodynamic variables at the boundaries are not

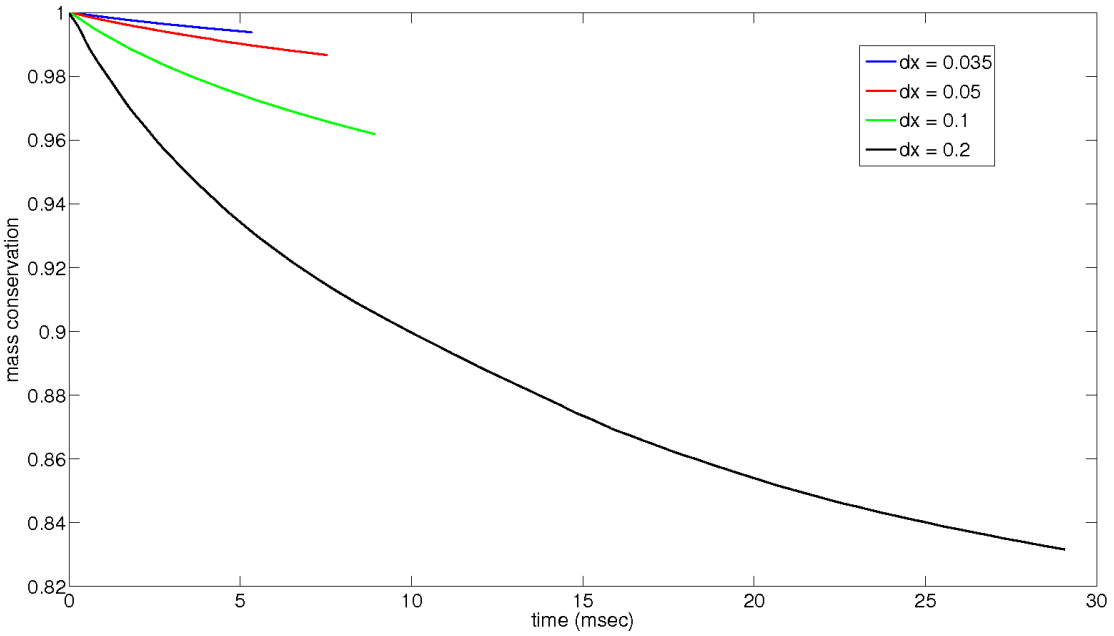

Figure 5.2: Disc mass conservation for different resolutions in Cowling approximation for model S_0975

evolved during the simulation. The Whisky2D code uses the Cactus interface for parallel computing and geometrical units (i.e. $c = G = 1$) with the mass unit being the solar mass. If not otherwise stated in the following all the quantities are expressed in these units.

To test this particular code against the system we want to study we followed a step by step procedure, first checking the stability in Cowling approximation, and then extending to the full-gr evolution that is what we need. The parameters and some physical quantities of the chosen model are in table 5.1. The system we are studying is made of a TOV star, surrounded by a stable torus (i.e. $\Delta W < 0$).

model	l_0	ΔW	r_{in}	r_{out}	$\rho_{c,disc}$	$\rho_{c,TOV}$
S_0975	3.99	-0.975	13.62	19.20	0.51×10^{-5}	1.8×10^{-3}

Table 5.1: Values of angular momentum, potential barrier, inner and outer radii of the disc and central density of the disc and of the TOV star

We choosed a disc deep inside the potential well to avoid spurious accretion due to numerical errors. We used 4 different resolutions for the runs in Cowling

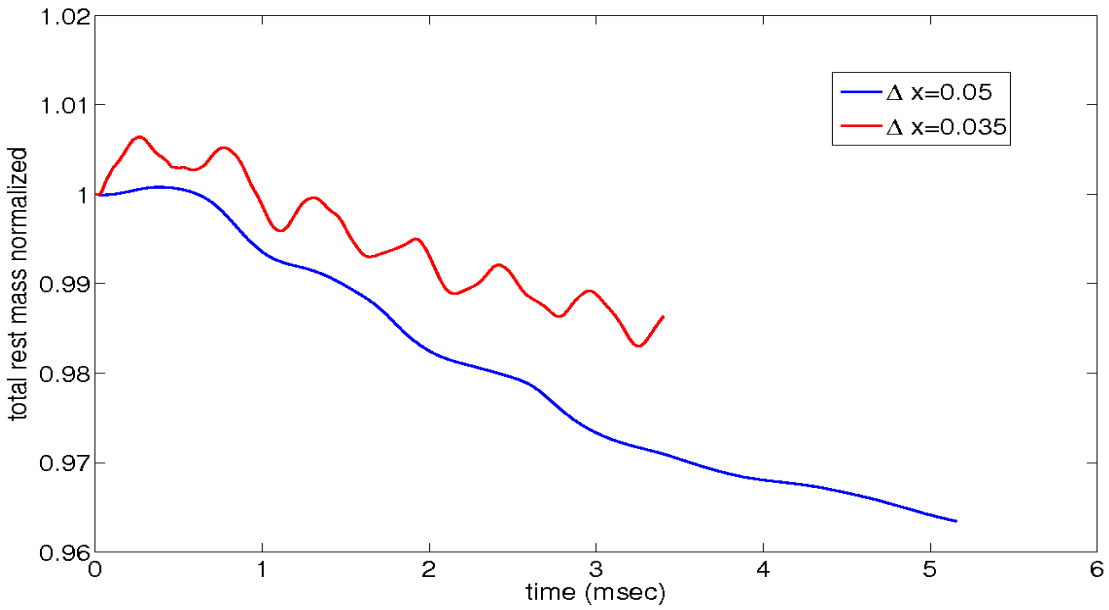

Figure 5.3: Disc mass conservation for different resolutions in full-gr for model S_0975

approximation and 2 in full-gr due to the much higher computational cost of this latter evolution scheme. Despite this better conservation of the disc mass, we don't find any sensible improvement in the overall mass due to the little absolute value of the disc mass. Besides this, our goal is to evolve accurately unstable discs in which a disc mass is not definite, so the most important quantities are the global ones. The reason why we made this simulations with stable models is to check that the disc does not evaporate due to low resolution and to check the reliability of the initial data. Thus the runs concerning unstable models will be done with a resolution of $\Delta x = 0.05$.

5.3 Evolution of the system

In this section we analize the results of runs in which the torus is generated in an unstable state to check the behaviour of the code in the accretion phase and to constrain the parameter space for collapse to be triggered. The quantities we want to measure are the amount of matter that can be accreted on the central TOV and how close to the stability limit its central density can be chosen not to trigger

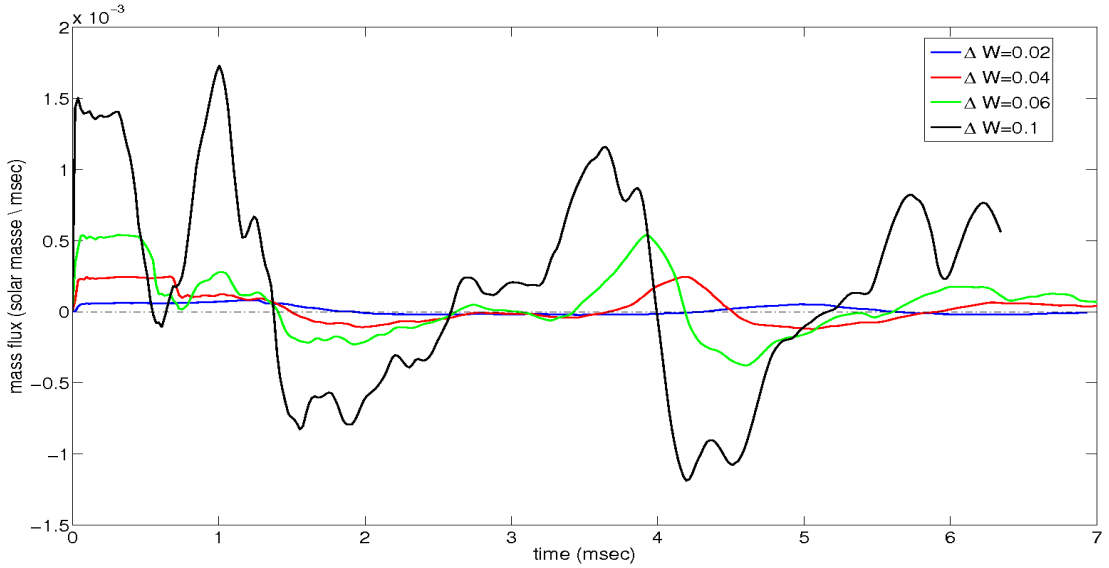

Figure 5.4: Mass flux through a spherical surface ($r = 6.8$) for different models

the collapse on its own. The two answers are related since the amount of matter that we need to trigger the collapse is directly proportional to the distance from the stability limit that we can reach with our numerical setup.

To estimate the amount of matter accreted and at the same time show the capability of the code to handle accretion we simulate 4 different models with different values of the parameter ΔW: $0.1, 0.06, 0.04, 0.02$. The star for these runs has a central density $\rho_c = 3 \times 10^{-3}$ that gives a sufficiently small star ($r_{eq} = 5.816$ with a mass of 1.637 solar masses) to keep the inner edge of the torus well separated from the surface of the star. The value of the central density is a first guess of a value that doesn't cause the collapse of the star without accretion. In figure 5.4 we show the mass accretion rate as a function of time computed with:

$$\dot{m} = 2\pi \int_0^{\pi} D v^r d\theta \tag{5.5}$$

where $D = gW\rho$ is the conserved density, g the spatial metric determinant, W the lorentz factor and v^r is the radial component of the 3-velocity of the fluid.

The flux is computed through a circle with radius $r = 6.8$. In this figure it is evident how the process of accretion on a TOV (and in general on a neutron star) is different from the one on a black hole. In this case the matter that is outside from the roche lobe, falling onto the star bounces on its surface and goes

model	U_002	U_004	U_006	U_010
ΔW	0.02	0.04	0.06	0.10
accreted matter	9.02×10^{-5}	1.56×10^{-4}	3.00×10^{-4}	1.10×10^{-3}

Table 5.2: Values of ΔW and of the total accreted matter after 6.3 msec for the models considered

back resulting in the oscillatory behaviour that is clear from the figure. The total amount of matter accreted for the different runs is summarized in table 5.2. The effect of the angular momentum left by the infalling matter on the star is the formation of a growing region (clearly visible in figures 5.5-5.7) inside the star in which the azimuthal velocity is not zero. In these figures below we plot the rest mass density in color scale (logarithmic) and the level surfaces for the azimuthal velocity v^{ϕ}, the model is U_010. The values of the velocities inside the star is quite small (the red line in figure marks the $v = 1 \times 10^{-5}$ surface) but nonetheless there's a considerable part of the star that starts to rotate.

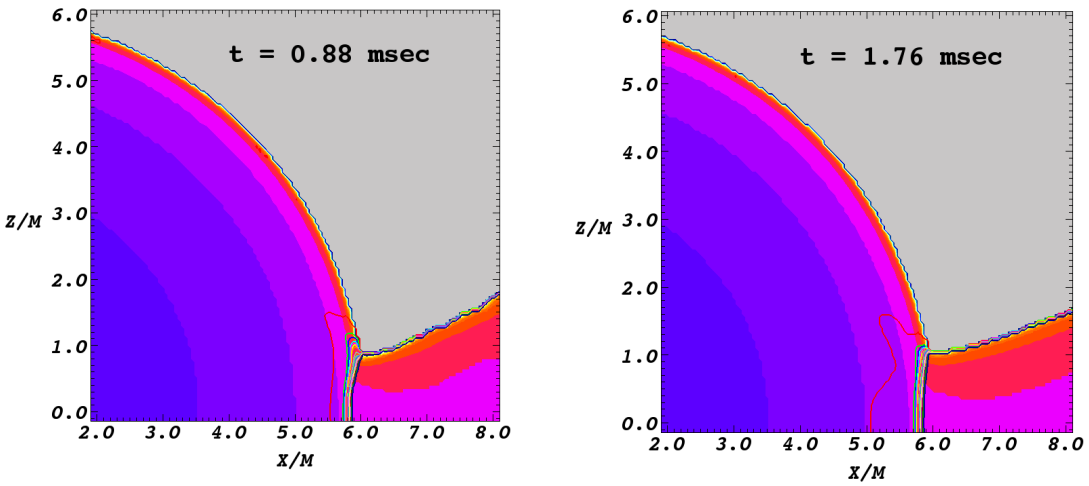

Figure 5.5: Snapshots of the rest mass density and azimuthal velocity in the z-x plane at $t = 0.88$ msec (left) and $t = 1.76$ msec (right). Color scale shows density, contour lines azimuthal velocity.

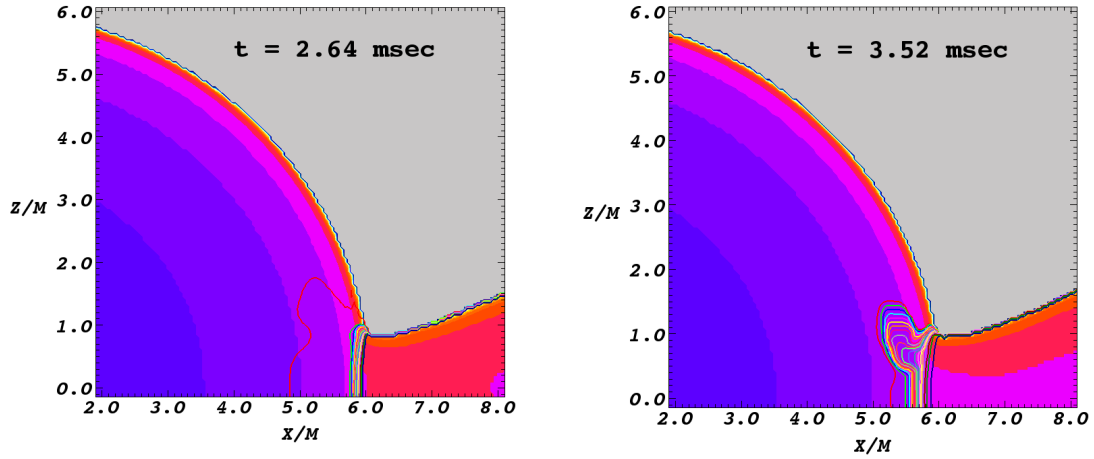

Figure 5.6: Snapshots of the rest mass density and azimuthal velocity in the z-x plane at $t = 2.64$ msec (left) and $t = 3.52$ msec (right). Color scale shows density, contour lines azimuthal velocity.

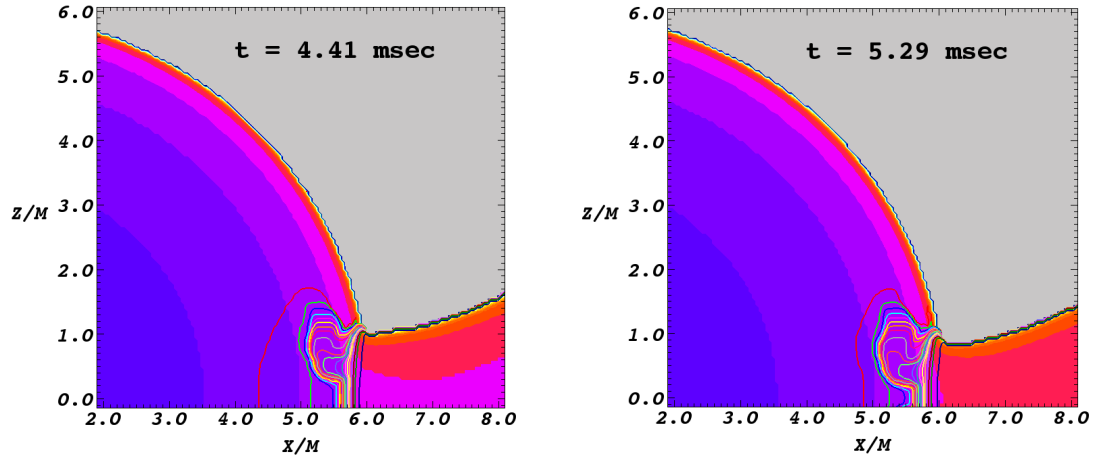

Figure 5.7: Snapshots of the rest mass density and azimuthal velocity in the z-x plane at $t = 4.41$ msec (left) and $t = 5.29$ msec (right). Color scale shows density, contour lines azimuthal velocity.

Chapter 6

Conclusions

In this thesis we studied the properties of two different systems, both capable to emit gravitational waves: differentially rotating neutron stars subject to the bar-mode instability and thick accretion discs around non rotating neutron stars.

Concerning the bar-mode instability, the plan of the work was to study the effect of a realistic equation of state on the features of the instability, namely on the dependence of the β parameter on the compactness of the star already studied for a polytropic equation of state. We simulated 4 models of differentially rotating neutron star, chosen to be around the threshold value for the polytropic EOS and with the highest possible value of β attainble with our initial data code. For all the four models we see a growth of the $m = 2$ mode, that becomes the dominant one, but the growth is not exponential as expected. This can be due to the EOS we are using or to the fact that the models are too close to the threshold value. More investigation of the parameter space by adding simulated models is needed to settle this point.

The deformation gained by the star and measured through the deformation parameter η is much lower than in the polytropic case, about 5 times lower. This causes the spiral arms that in the polytropic case were very pronounced to be very thin but still present and well definite. The frequency of the main mode of the $m = 2$ mode we extracted from η is between 2.22 and 2.42 kHz, depending on the model.

Even if the dynamics of the modes is not so clear it is possible to divide the evolution into phases that are common to all the models, with little deviations,

namely we have a first phase in which the star is dominated by the $m = 4$ deformation, a second phase in which the $m = 2$ and $m = 3$ cross it and stay on comparable values, the bar phase in which the $m = 2$ mode dominates and the phase where the dominant deformation is the $m = 3$. At the end we find that the $m = 1$ tends to grow and become the main deformation. With respect to the politropic case we have the difference that there was no $m = 3$ dominated part of the evolution.

We also found that the use of the direct fit $p = p(\rho)$, as in [34], of realistic EOSs is not suitable for numerical evolutions because it shows an anticonvergence problem in test runs on spherically symmetric neutron stars (probably due to the fact that this fit does not exactly fulfill the first principle of thermodynamics). We solved this problem by modifying the expression with which the pressure is computed according to [71].

Whether all these features we observe are due to the realistic EOS or to the fact that we are close to the threshold is a point that needs more investigation, also through the upgrading of code performances. In the future we plan thus to simulate more models and more equations of state, also of the non-isentropic type.

With respect to the thick accretion discs around non rotating neutron stars we tested toroughly the initial data code written by the author and found a satisfactory numerical setup. We simulated a number of accreting models to check the actual amount of matter that our discs can accrete and found this quantity to be around 1×10^{-3} that is enough to trigger a collapse. We observed in these runs an oscillatory behaviour in the mass flux through a spherical surface due to bounces of infalling matter on the star surface. Future plans involve the use of all this informations for actual collapse simulations and study of the effect of the accreting matter on the features of the collapse, namely the collapse timescale and the remnant.

Bibliography

[1] www.cactuscode.org.

[2] M. Abramowicz. The relativistic von zeipel's theorem. *ACTA ASTRONOMICA*, 21(1):81–85, 1971.

[3] M. Abramowicz. Theory of level surfaces inside relativistic, rotating stars. i. poincare's limit. *ACTA ASTRONOMICA*, 21(4):449–454, 1971.

[4] M. Abramowicz. Theory of level surfaces inside relativistic, rotating stars. ii. *ACTA ASTRONOMICA*, 24(1):45–53, 1974.

[5] M. Abramowicz, M. Jaroszyncki, and M. Sikora. Relativistic, accreting disks. *A&A*, 63:221–224, 1978.

[6] M. A. Abramowicz, M. Calvani, and L. Nobili. Runaway Instability in Accretion Disks Orbiting Black Holes. In B. Bertotti, F. de Felice, and A. Pascolini, editors, *General Relativity and Gravitation, Volume 1*, pages 677–+, July 1983.

[7] M. A. Abramowicz, V. Karas, and A. Lanza. On the runaway instability of relativistic tori. *A&A*, 331:1143–1146, Mar. 1998.

[8] M. Alcubierre. Appearance of coordinate shocks in hyperbolic formalisms of general relativity. *Phys.Rev.D*, 55:5981–5991, May 1997.

[9] M. Alcubierre, B. Brügmann, D. Pollney, E. Seidel, and R. Takahashi. Black hole excision for dynamic black holes. *Phys.Rev.D*, 64(6):061501–+, Sept. 2001.

[10] M. Alcubierre and J. Massó. Pathologies of hyperbolic gauges in general relativity and other field theories. *Phys.Rev.D*, 57:4511–+, Apr. 1998.

[11] L. Baiotti, S. Bernuzzi, G. Corvino, R. de Pietri, and A. Nagar. Gravitational-wave extraction from neutron-star oscillations: Comparing linear and nonlinear techniques. *Phys.Rev.D*, 79(2):024002–+, Jan. 2009.

[12] L. Baiotti, B. Giacomazzo, and L. Rezzolla. Accurate evolutions of inspiralling neutron-star binaries: Prompt and delayed collapse to a black hole. *Phys.Rev.D*, 78(8):084033–+, Oct. 2008.

[13] L. Baiotti, I. Hawke, P. J. Montero, and L. Rezzolla. A new three-dimensional general-relativistic hydrodynamics code. *Memorie della Societa Astronomica Italiana Supplement*, 1:210–+, 2003.

[14] L. Baiotti, R. D. Pietri, G. Manca, and L. Rezzolla. Accurate simulations of the dynamical bar-mode instability in full general relativity. *Phys.Rev.D*, 75:044023, 2007.

[15] J. G. Baker, J. Centrella, D.-I. Choi, M. Koppitz, and J. van Meter. Binary black hole merger dynamics and waveforms. *Phys.Rev.D*, 73(10):104002–+, May 2006.

[16] T. W. Baumgarte and S. L. Shapiro. Numerical integration of Einstein's field equations. *Phys.Rev.D*, 59(2):024007–+, Jan. 1999.

[17] S. Bernuzzi and A. Nagar. Gravitational waves from pulsations of neutron stars described by realistic equations of state. *Phys.Rev.D*, 78(2):024024, July 2008.

[18] C. Bona, J. Massó, E. Seidel, and J. Stela. New Formalism for Numerical Relativity. *Physical Review Letters*, 75:600–603, July 1995.

[19] J. Brown. Gravitational waves from the dynamical bar instability in a rapidly rotating star. *Phys.Rev.D*, 62:084024, 2000.

[20] M. Campanelli, C. O. Lousto, and Y. Zlochower. Last orbit of binary black holes. *Phys.Rev.D*, 73(6):061501–+, Mar. 2006.

[21] S. Chandrasekhar. *Ellipsoidal figures of equilibrium*. The Silliman Foundation Lectures, New Haven: Yale University Press, 1969, 1969.

[22] G. B. Cook, S. L. Shapiro, and S. A. Teukolsky. Rapidly rotating polytropes in general relativity. *ApJ*, 422:227–242, Feb. 1994.

[23] F. Daigne and J. Font. The runaway instability od thick discs around black holes - II. Non-constant angular momentum discs. *Mon.Not.R.Astron.Soc.*, 349:841–868, 2004.

[24] F. Daigne and R. Mochkovitch. Gamma-ray bursts and the runaway instability of thick discs around black holes. *Mon.Not.R.Astron.Soc.*, 285:L15–L19, Mar. 1997.

[25] P. Diener, F. Herrmann, D. Pollney, E. Schnetter, E. Seidel, R. Takahashi, J. Thornburg, and J. Ventrella. Accurate Evolution of Orbiting Binary Black Holes. *Physical Review Letters*, 96(12):121101–+, Mar. 2006.

[26] M. D. Duez, Y. T. Liu, S. L. Shapiro, and B. C. Stephens. Relativistic magnetohydrodynamics in dynamical spacetimes: Numerical methods and tests. *Phys.Rev.D*, 72(2):024028–+, July 2005.

[27] R. H. Durisen, R. A. Gingold, J. E. Tohline, and A. P. Boss. Dynamic fission instabilities in rapidly rotating N = 3/2 polytropes - A comparison of results from finite-difference and smoothed particle hydrodynamics codes. *ApJ*, 305:281–308, June 1986.

[28] L. Fishbone and V. Moncrief. Relativistic fluid disks in orbit around the kerr black hole. *ApJ*, 207:962–976, 1976.

[29] J. Font and F. Daigne. The runaway instability od thick discs around black holes - I. The constant angular momentum case. *Mon.Not.R.Astron.Soc.*, 334:383–400, 2002.

[30] J. A. Font. Numerical Hydrodynamics in General Relativity. *Living Reviews in Relativity*, 6:4–+, Aug. 2003.

[31] J. A. Font, J. M. Ibanez, A. Marquina, and J. M. Marti. Multidimensional relativistic hydrodynamics: Characteristic fields and modern high-resolution shock-capturing schemes. *ApJ*, 282:304–314, Feb. 1994.

[32] J. Frank, A. King, and D. J. Raine. *Accretion Power in Astrophysics: Third Edition*. Accretion Power in Astrophysics, by Juhan Frank and Andrew King and Derek Raine, pp. 398. ISBN 0521620538. Cambridge, UK: Cambridge University Press, February 2002., Feb. 2002.

[33] B. Giacomazzo and L. Rezzolla. WhiskyMHD: a new numerical code for general relativistic magnetohydrodynamics. *Classical and Quantum Gravity*, 24:235–+, June 2007.

[34] P. Haensel and A. Potekhin. Analytical representations of unified equations of state of neutron-star matter. *A&A*, 428:191–197, Dec. 2004.

[35] J. Houser, J. Centrella, and S. Smith. Gravitational radiation from non-axysimmetric instability in a rotating star. *Phys.Rev.Lett.*, 72(9):1314–1317, Feb. 1994.

[36] J. L. Houser and J. M. Centrella. Gravitational radiation from rotational instabilites in compact stellar cores with stiff equations of state. *Phys.Rev.D*, 54:7278–7297, Dec. 1996.

[37] S. Karino and Y. Eriguchi. Linear Stability Analysis of Differentially Rotating Polytropes: New Results for the m=2 f-Mode Dynamical Instability. *ApJ*, 592:1119–1123, Aug. 2003.

[38] T. Kellerman, L. Baiotti, B. Giacomazzo, and L. Rezzolla. An improved formulation of the relativistic hydrodynamics equations in 2D Cartesian co-ordinates. *Classical and Quantum Gravity*, 25(22):225007, Nov. 2008.

[39] R. Khanna and S. K. Chakrabarti. Effects of a self-gravitating disc on test particle motion around a Kerr black hole. *Mon.Not.R.Astron.Soc.*, 259:1–5, Nov. 1992.

[40] H. Komatsu, Y. Eriguchi, and I. Hachisu. Rapidly rotating general relativistic stars. I - Numerical method and its application to uniformly rotating polytropes. *Mon.Not.R.Astron.Soc.*, 237:355–379, Mar. 1989.

[41] H. Komatsu, Y. Eriguchi, and I. Hachisu. Rapidly rotating general relativistic stars. II - Differentially rotating polytropes. *Mon.Not.R.Astron.Soc.*, 239:153–171, July 1989.

[42] M. Kozlowsky, M. Jaroszyncki, and M. Abramowicz. The analytic theory of fluid disks orbiting the kerr black hole. *A&A*, 63:209–220, 1978.

[43] G. Lavagetto, L. Burderi, F. D'Antona, T. Di Salvo, R. Iaria, and N. R. Robba. The different fates of a low-mass X-ray binary - I. Conservative mass transfer. *Mon.Not.R.Astron.Soc.*, 348:73–82, Feb. 2004.

[44] G. Lavagetto, L. Burderi, F. D'Antona, T. di Salvo, R. Iaria, and N. R. Robba. The role of general relativity in the evolution of low-mass X-ray binaries. *Mon.Not.R.Astron.Soc.*, 359:734–740, May 2005.

[45] D. N. C. Lin and J. C. B. Papaloizou. Theory of Accretion Disks II: Application to Observed Systems. *Ann.Rev.Astron.Astroph.*, 34:703–748, 1996.

[46] Y. T. Liu. Dynamical instability of new-born neutron stars as sources of gravitational radiation. *Phys.Rev.D*, 65(12):124003–+, June 2002.

[47] Y. Lu, K. S. Cheng, L. T. Yang, and L. Zhang. A massive thick disc around a massive black hole and its runaway instability. *Mon.Not.R.Astron.Soc.*, 314:453–458, May 2000.

[48] G. Manca, L. Baiotti, R. D. Pietri, and L. Rezzolla. Dynamical non-axisymmetric instabilities in rotating relativistic stars. *Classical and Quantum Gravity*, 24:S171–S186, 2007.

[49] N. Masuda, S. Nishida, and Y. Eriguchi. The runaway instability of self-gravitating tori with non-constant specific angular momentum around black holes. *Mon.Not.R.Astron.Soc.*, 297:1139–1144, July 1998.

[50] P. Mészáros. The fireball shock model of gamma ray bursts. In S. S. Holt and W. W. Zhang, editors, *American Institute of Physics Conference Series*, volume 522 of *American Institute of Physics Conference Series*, pages 213–225, 2000.

[51] P. M. Motl, M. Anderson, E. W. Hirschman, L. Lehner, S. L. Liebling, D. Neilsen, C. Palenzuela, and J. E. Tohline. Fully Relativistic Simulations of the Merger and Collapse of Neutron Star Binaries. In *Bulletin of the American Astronomical Society*, volume 38 of *Bulletin of the American Astronomical Society*, pages 949–+, Dec. 2007.

[52] T. Nakamura, K. Oohara, and Y. Kojima. General Relativistic Collapse to Black Holes and Gravitational Waves from Black Holes. *Progress of Theoretical Physics Supplement*, 90:1–218, 1987.

[53] R. Narayan and I. Yi. Advection-dominated accretion: A self-similar solution. *ApJL*, 428:L13–L16, June 1994.

[54] R. Narayan and I. Yi. Advection-dominated accretion: Self-similarity and bipolar outflows. *ApJ*, 444:231–243, May 1995.

[55] K. New and S. Shapiro. Evolution of differentially rotating supermassive stars to the onset of bar instability. *ApJ*, 548:439–446, Jan. 2001.

[56] K. C. B. New, J. M. Centrella, and J. E. Tohline. Gravitational waves from long-duration simulations of the dynamical bar instability. *Phys.Rev.D*, 62(6):064019–+, Sept. 2000.

[57] S. Nishida, A. Lanza, Y. Eriguchi, and M. A. Abramowicz. Runaway instability and gamma-ray bursts. *Mon.Not.R.Astron.Soc.*, 278:L41–L45, Feb. 1996.

[58] R. Oechslin, H.-T. Janka, and A. Marek. Relativistic neutron star merger simulations with non-zero temperature equations of state. I. Variation of binary parameters and equation of state. *ApJ*, 467:395–409, May 2007.

[59] C. D. Ott, S. Ou, J. E. Tohline, and A. Burrows. One-armed Spiral Instability in a Low-T/|W| Postbounce Supernova Core. *ApJL*, 625:L119–L122, June 2005.

[60] B. K. Pickett, R. H. Durisen, and G. A. Davis. The Dynamic Stability of Rotating Protostars and Protostellar Disks. I. The Effects of the Angular Momentum Distribution. *ApJ*, 458:714–+, Feb. 1996.

[61] F. Pretorius. Simulation of binary black hole spacetimes with a harmonic evolution scheme. *Classical and Quantum Gravity*, 23:529–+, Aug. 2006.

[62] M. Saijo, T. W. Baumgarte, and S. L. Shapiro. One-armed Spiral Instability in Differentially Rotating Stars. *ApJ*, 595:352–364, Sept. 2003.

[63] M. Saijo, M. Shibata, T. Baumgarte, and S. Shapiro. Dynamical Bar Instability in Rotating Stars: Effect of General Relativity. *ApJ*, 548:919–931, Feb. 2001.

[64] N. I. Shakura and R. A. Syunyaev. Black holes in binary systems. Observational appearance. *ApJ*, 24:337–355, 1973.

[65] S. L. Shapiro and S. A. Teukolsky. *Black holes, white dwarfs, and neutron stars: The physics of compact objects*. Research supported by the National Science Foundation. New York, Wiley-Interscience, 1983, 663 p., 1983.

[66] M. Shibata, S. Karino, and Y. Eriguchi. Dynamical instability of differentially rotating stars. *Mon.Not.R.Astron.Soc.*, 334:L27–L31, Aug. 2002.

[67] M. Shibata, S. Karino, and Y. Eriguchi. Dynamical bar-mode instability of differentially rotating stars: effects of equations of state and velocity profiles. *Mon.Not.R.Astron.Soc.*, 343:619–626, Aug. 2003.

[68] M. Shibata and T. Nakamura. Evolution of three-dimensional gravitational waves: Harmonic slicing case. *Phys.Rev.D*, 52:5428–5444, Nov. 1995.

[69] M. Shibata and Y.-I. Sekiguchi. Magnetohydrodynamics in full general relativity: Formulation and tests. *Phys.Rev.D*, 72(4):044014–+, Aug. 2005.

[70] M. Shibata and K. Taniguchi. Merger of binary neutron stars to a black hole: Disk mass, short gamma-ray bursts, and quasinormal mode ringing. *Phys.Rev.D*, 73(6):064027–+, Mar. 2006.

[71] M. Shibata, K. Taniguchi, and K. Uryū. Merger of binary neutron stars with realistic equations of state in full general relativity. *Phys.Rev.D*, 71(8):084021, Apr. 2005.

[72] L. Smarr and J. J. W. York. Kinematical conditions in the construction of spacetime. *Phys.Rev.D*, 17:2529–2551, May 1978.

[73] S. C. Smith, J. L. Houser, and J. M. Centrella. Simulations of Nonaxisymmetric Instability in a Rotating Star: A Comparison between Eulerian and Smooth Particle Hydrodynamics. *ApJ*, 458:236–+, Feb. 1996.

[74] H. Sotani, K. D. Kokkotas, and N. Stergioulas. Torsional oscillations of relativistic stars with dipole magnetic fields. *Mon.Not.R.Astron.Soc.*, 375:261–277, Feb. 2007.

[75] H. Sotani, K. D. Kokkotas, and N. Stergioulas. Alfvén quasi-periodic oscillations in magnetars. *Mon.Not.R.Astron.Soc.*, 385:L5–L9, Mar. 2008.

[76] N. Stergioulas and J. L. Friedman. Comparing models of rapidly rotating relativistic stars constructed by two numerical methods. *ApJ*, 444:306–311, May 1995.

[77] N. Straumann. *General relativity with applications to astrophysics*. General relativity with applications to astrophysics, by Norbert Straumann. Springer Texts and monographs in physics. Berlin: Springer, 2004, 2004.

[78] J. Tohline, R. Durisen, and M. McCollough. The linear and nonlinear dynamic stability of rotating n=3/2 polytropes. *ApJ*, 298:220–234, Nov. 1985.

[79] J. E. Tohline and I. Hachisu. The breakup of self-gravitating rings, tori, and thick accretion disks. *ApJ*, 361:394–407, Oct. 1990.

[80] D. B. Wilson. A runaway instability in thick accretion disks? *Nature*, 312:620, Dec. 1984.